University of Utah Interlibrary Loan

ILLiad TN: 199078

July 6, 2005

Borrower: UBY

Lending String: *UUM,UUM,IXA,LDL,OKS

Patron: Peterson, Bryan

Journal Title: International journal of mass spectrometry and ion processes.

Volume: 165-166 **Issue:** November
Month/Year: 1997 **Pages:** 271-297

Article Author:

Article Title: Dale W. Mitchell and Richard D. Smith; Two dimensional many particle simulation of trapped ions

Imprint: Amsterdam ; Elsevier, c1983-c1998.

ILL Number: 10556679

Location:

ARIEL
Charge
Maxcost: 35IFM

Shipping Address:
BRIGHAM YOUNG UNIVERSITY
3421 LEE LIBRARY ILL
ONE LEE LANE
PROVO UT 84602

Fax: 801-422-0471
Ariel: provoariel.lib.byu.edu

ELSEVIER International Journal of Mass Spectrometry and Ion Processes 165/166 (1997) 271–297

International Journal of Mass Spectrometry and Ion Processes

Two dimensional many particle simulation of trapped ions

Dale W. Mitchell[a], Richard D. Smith[b,*]

[a] *Department of Physics and Astronomy, Ohio University, Athens, OH 45701, USA*
[b] *Pacific Northwest National Laboratory, Environmental Molecular Science Laboratory, P.O. Box 999, M.S. P8-19, Richland, WA 99352, USA*

Received 3 October 1996; accepted 12 June 1997

Abstract

This work describes the implementation of the particle-in-cell simulation method with Monte-Carlo Langevin and hard sphere ion-neutral collisions in our two dimensional Cartesian and cylindrical coordinate system codes. The particle-in-cell method efficiently and accurately solves complex dynamics involving many interacting particles. In our case 'many' means simulation runs with thousands to tens of thousands of Coulombically interacting particles on a workstation. In addition, the image charge induced on the device electrodes, which is required for self-consistency in order to make the electrodes equipotentials, is incorporated with this method. For an azimuthally symmetric confinement geometry and charge distribution, results using the two dimensional cylindrical (rz) particle simulator are identical to full three-dimensional simulations, by symmetry. These codes are applied to a number of examples which are relevant to trapped ion mass spectrometry in order to demonstrate their utility. Computer experiments are carried out to study the maximum number of ions which can be confined and equilibrium cloud shapes in cylindrical ICR traps, ion cloud collisional cooling in a combined trap, merger of two off-axis charge columns, Kelvin-Helmholtz instability in ring-shaped initial distributions, vortex crystallization, and image charge detection of coherent cyclotron motion. © 1997 Elsevier Science B.V.

Keywords: Non-neutral plasma; Fourier transform mass spectrometry; Ion trap; Plasma simulation

---

1. Introduction

Realistic many particle simulations not only provide insights into the various complexities associated with high space charge conditions in trapped ion mass spectrometry, they also can be used to guide the design of optimal instrumentation and experimental sequences. It is usually much easier and less expensive to modify the computer code than the experimental apparatus. In addition, while most experiments rely on just

---

* Corresponding author. E-mail: rd – smith@pnl.gov

PII S0168-1176(97)00170-5

one or at most a few diagnostic tools, such as image charge detection in Fourier transform mass spectrometry or resonance ejection in quadrupole ion traps, which allows the experimenter to observe limited information on the ion ensemble, a realistic computer experiment visualizes directly all major aspects of ion cloud evolution.

Extensive simulation work has been carried out to investigate ion dynamics in quadrupole and ICR ion traps [1–12]. In nearly all previous simulation work applied to mass analyzers the trajectory of a single ion or a relatively small number of interacting particles is followed through time in the presence of externally applied electric and magnetic fields. The most widely employed simulation method for mass analyzers and ion optical devices is a few ion approach where the ion-ion interactions, if included at all, are derived by directly summing the N^2 Coulomb forces, where N is the number of interacting particles. Calculating Coulombic effects by summing directly the particle–particle interactions is generally impracticable for large numbers of particles due to the N^2 scaling of the Coulomb force calculation. Several different efficient computational algorithms are available for the efficient solution of the N-body problem, the two most important of which are tree codes [13] and the particle-in-cell (alternatively called particle-mesh) method [14–19]. Both of these methods yield an efficient, though approximate, solution of the actual N-body problem. A comparison of different N-body methods to ion trajectory calculations is beyond the scope of the present paper. The particle-in-cell method has been chosen for this study since this approach is a widely employed and standard method in computational plasma physics. In particular the method is well tested and proven reliable in making quantitative predictions for plasma properties. One expects that the particle-in-cell method is capable of yielding quantitatively accurate results for mass spectrometry simulations based on its previous successes in modeling complex plasma behavior. The particle-in-cell simulation method (PIC) efficiently solves the Coulombic many body problem by replacing the direct particle–particle summation with the introduction of a spatial grid to calculate the potential, including space charge, and the introduction of finite-sized particles.

PIC originally was developed for fluid dynamics simulations [14]; however, its greatest application is in plasma physics where the collective behavior in a system with density of typically 10^{12} cm^{-3} for laboratory plasmas needs to be simulated. There are excellent books and reviews written on particle-in-cell simulations applied to various plasma physics problems [15–19]. PIC simulations are also employed in gravitational systems such as galactic simulations [19,20]. Of more direct relationship to this work, PIC has been applied to a variety of non-neutral plasma physics problems. A two-dimensional slab equivalent to a Penning-Malmberg trap has previously been employed to investigate equilibrium properties, cross-field transport by neutral collisions, solitons arising from initial disturbances and ion crystallization [21]. The particle-in-cell method has recently been used to study the normal modes of a cold charged cloud in a Penning trap, including temperature dependencies [22]. Early on, Hockney successfully simulated the formation of virtual electrodes which develop when several electron guns, positioned symmetrically opposed at the edge of a conducting cylindrical tube, are directed towards the tube's center [23].

This work describes the implementation of the PIC algorithm in our two-dimensional cylindrical and Cartesian codes. These codes are tested and their utility demonstrated by a number of examples which are relevant to trapped ion mass spectrometry at high space charge conditions. The extension to three dimensions is straightforward, though more computationally intensive, and will be described elsewhere. The real world is three dimensional; therefore, we must be careful in applying two dimensional numerical results to actual three dimensional devices. Nonetheless, there are several reasons why two dimensional simulations are relevant and interesting in the regime where space charge effects are important. The inclusion of realistic space charge effects in two and three dimensional geometries generally makes an exact analytical solution impossible. Therefore, one relies on an approximate analytical treatment which should be tested by experimental results whenever such experiments are available. On the other hand, an accurate computer simulation is a viable alternative to actual laboratory-based experiments if the important dynamical effects are properly treated. Therefore, one important role of computer experiments is to test correctness of the approximate analytical models. Symmetry simplifies many kinds of problems. For example, if the confinement geometry and the charge distribution are axially symmetric then two-dimensional simulations using a cylindrical *rz* coordinate system are identical to full three dimensional simulations. Some of our two-dimensional simulations deal with this cylindrical geometry and are, therefore, identical to what one would obtain using a full three-dimensional PIC code with much less computational effort. In addition there are important two-dimensional problems that have not yet been solved. It is well known, and recently exploited by plasma physicists, that the equations of motion governing the two-dimensional $E \times B$ drift dynamics of charge columns are isomorphic to the Euler equations for a two-dimensional incompressible inviscid fluid [24]. An intense area of current research is directed at trying to understand two dimensional turbulence in the Euler equations and to exploit the fluid analogy by making precise fluid measurements through non-neutral plasma experiments [24–27].

This paper is organized as follows: firstly, the computational algorithm implemented in our two dimensional Cartesian and cylindrical coordinate system particle-in-cell simulator, is described. In the Sec. 3 these codes are applied to different physical situations of interest to trapped ion mass spectrometry and/or non-neutral plasma physics experiments. The cylindrical *rz* code is applied to a cylindrically symmetric confinement geometry containing a cylindrically symmetric charge distribution. Therefore, while the *rz* code is two-dimensional, the results obtained below using this code should be identical to a full three-dimensional simulation, by symmetry. Problems studied using the cylindrical PIC code include determination of the maximum charge which can be contained in a cylindrical Penning trap and collisional cooling of an ion cloud in a combined trap. This is followed by applying the Cartesian *xy* code to a number of interesting physical situations. A pure electron plasma confined by a Penning-Malmberg trap, whose length is much greater than its radius, exhibits nearly two dimensional dynamics perpendicular to the applied magnetic field [24]. In addition, at high ion density, the electric field along the z-axis is nearly cancelled by the space charge electric field even in a small aspect ratio Penning trap, resulting in essentially two-dimensional (xy) ion trajectories for those situations. We apply the Cartesian *xy* particle-in-cell simulator to charged columns in a number of initial configurations leading to interesting dynamics. Vortex merger and the Kelvin-Helmholtz instability are demonstrated with two off-axis charge columns and ring ion clouds, respectively. Comparison is made between computer simulation with available experimental data and analytical models. Other simulations include image charge detection of coherent cyclotron motion and the first computer simulation of the recently discovered phenomenon of vortex crystallization [27].

2. Computational procedure

PIC is capable of following the dynamics of tens of thousands of interacting particles on workstations ($> 10^6$ on a supercomputer [16]) with self-consistent fields. Most simulation work on ion dynamics in ICR Penning traps, rf Paul traps or combined traps either neglect space charge effects completely or include the ion-ion interactions by directly summing the Coulomb interactions between a few particles. The major problem with this approach is that computational effort scales as order N^2. Even high performance vector and parallel computers are limited to a maximum of ~ 1000 particles for several thousand time steps if this approach is taken [7,12]. PIC is an $O(N)$ method, which lets one treat thousands of interacting particles with relatively modest computing resources. With the PIC method the space charge electric field is calculated at the ion positions, not by summing the N^2 Coulomb forces, but rather from a computational grid on which force is zero for completely overlapping clouds [11,33]. Treating superparticles as finite size ion clouds is intuitively reasonable since there is a maximum density achievable for the ion clouds [34]. The particle-in-cell method implicitly incorporates finite size particles in the algorithm [16,32].

After various inputs are chosen (including the device geometry, applied potentials and fields, number of simulation particles, their masses, charges, initial positions and initial velocities) the simulation follows the PIC algorithm outlined in Fig. 1. The interior of the trap is divided into a computational mesh. Field quantities are evaluated on the grid points of this computational mesh. In the most general PIC algorithms the full Maxwell equations are solved including self-magnetic fields and relativity; however, in our implementation we use the electrostatic approximation which neglects relativistic effects and self-magnetic fields [15]. Fully electromagnetic PIC simulators find their greatest application when radiation is of interest, such as in the study of laser-plasma interactions; or at very high temperatures and density, such as in fusion plasmas. In nearly all problems of interest to mass spectrometrists the electrostatic approximation is excellent.

At each time step in the PIC simulation the fields are derived and the particles advanced according to the following procedure: charge density is assigned to the grid points of the computational mesh using bilinear interpolation from the particle positions to the four nearest grid points to each particle. The potential is solved exactly at the grid points by direct solution of Poisson's equation. The electric field is calculated at each particle position by interpolation from the electric field of the nearest four grid points. The same weighting scheme is used as for the charge density. The particle positions and velocities are advanced in time for one time step by the explicit second-order leap frog method [15,19]. In cases where a collision gas is included, ion-neutral elastic collisions are incorporated by the Monte-Carlo method. Any particles which are found to have hit an electrode are removed from the simulation. The process is repeated for the next time step. During the course of a simulation run, selected frames are recorded for a movie and various histories are recorded, such as total energy, electrostatic energy, canonical angular momentum about the magnetic field, and image charge induced on a particular electrode. Below, the separate steps in the PIC algorithm, as implemented in our codes, are described in detail. The codes are written in FORTRAN and C and currently run on a variety of Unix workstations and PCs. Work is in progress towards developing a graphical user interface with cross-platform capability and the development of a suite of general purpose two- and three-dimensional electrostatic particle-in-cell simulation codes.

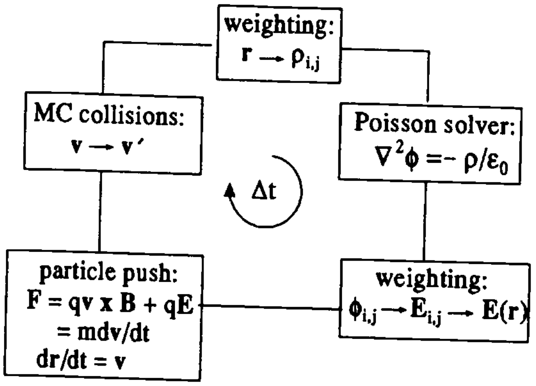

Fig. 1. Graphical representation of the particle-in-cell simulation algorithm.

2.1. Area weighting: interpolate particle positions to charge density at the grid points

The first part of the PIC algorithm is to set up the charge density matrix ρ which is required for the Poisson solver. Since Poisson's equation is solved on a computational mesh, the charge density needs to be known at the grid points; however, the particles are free to be anywhere in space. Therefore, one must interpolate charge density from the ion positions to the computational grid. Our codes implement the widely used bilinear weighting, also known as particle-in-cell or area weighting [15–17]. Fig. 2 demonstrates area weighting for a 2D Cartesian grid. The particle is located inside of a computational mesh cell at position x,y and only the four nearest grid points, labeled 1 to 4, are shown. The dimensionless weights w_1 to w_4 are the areas of the indicated regions divided by the area of one mesh cell, so that the sum of the weights equals one, i.e. $w_1 + w_2 + w_3 + w_4 = 1$. The charge density associated with any given particle is distributed to its four nearest grid points according to these weights. For example, if the mesh cell has width h and the charge per unit length for one particle is Q/L, then the charge density assigned to grid point k ($k = 1,2,3,4$) in Fig. 2 due to the particle located at coordinate x,y is given by $w_k Q/h^2 L$. Repeating this procedure for all of the particles, results in the total charge density matrix $\rho_{i,j}$, where i and j are indices for the 2D Cartesian xy computational grid. For the cylindrical coordinate (rz) PIC code, the same area weighting scheme is employed to weight each simulation particle to its four neighboring grid points. However, the density calculation is modified in order to take into account that the volume for one mesh cell is r-dependent according to $\pi h^3/4$, for $j = 1$ corresponding to $r = 0$, and $\pi h^3(2j-2)$, for $j > 1$, where j is the grid indice in the radial cylindrical direction, instead of $h^2 L$ used in the Cartesian xy code.

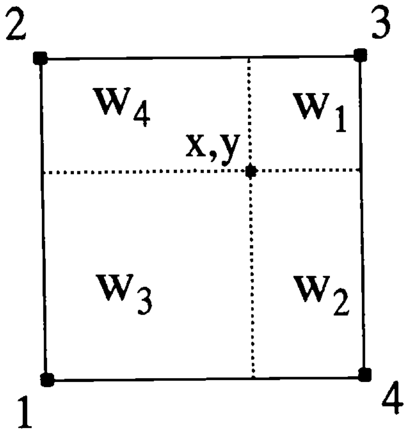

Fig. 2. The area weighting scheme for a Cartesian grid used for interpolating between particle positions and grid quantities (ρ and E). Only the four nearest grid points to a simulation particle located at position x,y are indicated. The charge density at grid points labeled 1 through 4 is interpolated from the particle located at x,y by assigning the weights w_1 through w_4 to the respective grid points. The dimensionless weights are the areas of the indicated regions divided by h^2, the area of one mesh cell. The area weighting scheme is used for both interpolating charge at particle positions to charge density at grid points and interpolating electric field at grid points to the particle positions.

Since charge is distributed to neighboring grid points, the area weighting scheme has the effect of introducing finite size particles, rather than point particles, into the simulation. The physics of finite-sized particles is well developed [15–17]. The 2D xyPIC code (no variation of the fields in the z direction) essentially replaces each line charge particle with an approximately uniform charge density rod whose cross-sectional area is h^2. In the 2D cylindrical rzPIC code (no azimuthal variation), the simulation particles are approximately uniformly charged rings of cross-sectional area h^2. The singularity associated with the Coulomb interaction between point particles is removed implicitly in PIC simulations.

2.2. Poisson solver: determination of the potential from the density matrix

The electrostatic potential Φ (space charge + image charge + trap potential) is derived by the numerical solution of Poisson's equation $\nabla^2\Phi = -\rho/\varepsilon_0$ on the computational grid, where $\varepsilon_0 = 8.85 \times 10^{-12}$ F m^{-1} is the vacuum permittivity and ρ is the charge density. The method is self-consistent since Poisson's equation is solved at each time step in the simulation. The PIC method is efficient owing to the availability of very fast methods for solving the finite difference form of Poisson's equation [18,35]. In our PIC codes we employ the direct, non-iterative Poisson solvers of Schwartzrauber and Sweet which rapidly solve Poisson's equation to full machine precision using cyclic reduction [36,37]. These Poisson solvers are sufficiently general to handle any combination of Dirichlet (potentials specified on the boundary), Neumann (electric field specified at the boundary) or periodic boundary conditions. The direct Poisson solvers yield an exact solution of the finite difference Poisson equation, accurate to full machine precision.

As examples of the efficiency of the Poisson

---

solvers implemen
given for an IB
direct solution o
Cartesian 64 × 6
meshes required
respectively. Th
equation on cyli
200 computation
0.118 s CPU, res

In comparison
overrelaxation m
employed here a
magnitude faster.
between the dire
successive overre
and 128 × 128 c
Poisson solver wa
the overrelaxatio
128 × 128 grids,
criteria of 10^{-5}
method. On the
solver yielded the
rate to machine
the overrelaxatio
are required,
method is even
rect Poisson solve
computational
O(N_g Log N_g), wh
points in the co
much more effic
ation whose comp
[18].

Without modifi
are only applica
geometries where
with the electrode
ble for a cylindri
nate system Poiss
trap if a Cartesi
ployed. However,
any arrangement
direct solvers by
method [18,23]. W
matrix method in
potential correct
forces arising fr
rangements. In

solvers implemented in our codes, CPU times are given for an IBM-RISC 6000 workstation. The direct solution of Poisson's equation on 2D (xy) Cartesian 64×64 and 128×128 computational meshes required 0.016 s and 0.072 s CPU time, respectively. The direct solution of Poisson's equation on cylindrical (rz) 64×128 and 100×200 computational meshes required 0.038 s and 0.118 s CPU, respectively, on a RISC 6000.

In comparison to the more familiar successive overrelaxation method, the direct Poisson solvers employed here are approximately three orders of magnitude faster. A timing comparison was made between the direct Cartesian Poisson solver and successive overrelaxation for Cartesian 64×64 and 128×128 computational grids. The direct Poisson solver was 400 and 1000 times faster than the overrelaxation method for the 64×64 and 128×128 grids, respectively, using a convergence criteria of 10^{-5} error for the overrelaxation method. On the other hand, the direct Poisson solver yielded the finite difference solution accurate to machine precision. If higher accuracy (in the overrelaxation method) or larger grid sizes are required, the successive overrelaxation method is even more inefficient compared to direct Poisson solvers. Direct Poisson solvers have a computational efficiency that scales as $O(N_g \mathrm{Log} N_g)$, where N_g is the number of grid points in the computational mesh [18]. This is much more efficient than successive overrelaxation whose computational effort scales as $O(N_g^2)$ [18].

Without modification the direct Poisson solvers are only applicable to the special electrode geometries where the coordinate system coincides with the electrode boundary, i.e. are only applicable for a cylindrical trap if a cylindrical coordinate system Poisson solver is employed or a box trap if a Cartesian system direct solver is employed. However, it is possible to accommodate any arrangement of interior electrodes with the direct solvers by use of the capacitance matrix method [18,23]. We have included the capacitance matrix method in our codes in order to have the potential correct everywhere, including image forces arising from complicated electrode arrangements. In the capacitance matrix method Poisson's equation is first solved without any interior electrodes. All of the error potentials (differences between desired potentials at the interior electrode points and the actual potentials) are recorded then multiplied by a pre-calculated capacitance matrix which gives charge at each interior electrode required to give the correct electrode potential. Poisson's equation is solved a second time with the charge at the interior electrode points. The resulting potential is correct everywhere including the interior electrodes. Therefore, at the expense of having to solve Poisson's equation twice per time step the direct Poisson solvers are applicable to any arrangement of interior electrodes.

2.3. *Area weighting: interpolate potential at grid points to electric field at ion positions*

The electric field at the grid points is evaluated numerically by differentiating the potential at the grid points using central differences. For example, if i is the indice of the grid in the x direction, then the x component of the electric field at grid point i,j is given by $E_x \cong -(\Phi_{i+1,j} - \Phi_{i-1,j})/2h$ which is valid to second order in h, the distance between nearest neighbor grid points. The electric field at electrode boundaries is calculated by first-order differences. The electric fields at all particle positions are calculated by interpolating from the electric field at the grid points using the same area weighting scheme as described above for the calculation of the charge density matrix.

2.4. *Particle push: moving the particles forward in time for one time step*

The particles are pushed forward in time for a single step Δt by solving the Newton equation with Lorentz force. For a single particle of mass m, charge q, position r, velocity v, in a magnetic field B and electric field E,

$$m\frac{dv}{dt} = qv \times B + qE$$
$$\frac{dr}{dt} = v \qquad (1)$$

These equations are numerically integrated at a constant time step by using the second-order explicit leap-frog scheme, a widely employed and surprisingly accurate integration procedure [15,19,38]. While the PIC codes described here are two-dimensional, all three velocity components are evaluated in order to treat elastic ion-neutral collisions which involves all three velocity components. The leap-frog method originally was derived heuristically based on the desirability of obtaining very fast numerical algorithms which are time reversible and time centered [38]. Algorithms possessing these qualities are generally stable for a sufficiently small time step and do a good job conserving certain properties, such as total energy and canonical angular momentum about the magnetic field in ICR traps. The leap-frog equations of motion are [15–19]

$$m\frac{v^{t+\Delta t/2}-v^{t-\Delta t/2}}{\Delta t}=q\frac{v^{t+\Delta t/2}+v^{t-\Delta t/2}}{2}\times B^t+qE^t\frac{r^{t+\Delta t}-r^t}{\Delta t}=v^{t+\Delta t/2} \qquad (2)$$

where the superscripts denote the time at which the respective position r, velocity v, electric and magnetic fields are evaluated. Notice that r and v are staggered in time by $\Delta t/2$. Given particle positions at time t and velocities at time $t-\Delta t/2$, the leap-frog returns positions and velocities at times $t+\Delta t$ and $t+\Delta t/2$, respectively. The leap-frog scheme is stable provided that the product of the fastest angular frequency ω present in the physical system and the time step Δt is less than two (i.e. numerical stability requires $\omega\Delta t<2$) [19]. In most of our simulations, the fastest angular frequency is the cyclotron frequency.

The leap-frog scheme is used for all times; however, the leap-frog method is not self-starting since the algorithm requires r ($t=\Delta t/2$), in addition to v ($t=0$). Given particle initial conditions r^0 and v^0 the leap-frog method is made self-starting in our codes by integrating r in time for the first one-half time step using the elementary algorithm [1]

$$r^{\Delta t/2}=r^0+\frac{v^0\Delta t}{2}+\frac{q\,\Delta t^2}{8m}(v\times B+E)^0 \qquad (3)$$

After using this elementary algorithm for the first one-half time step, the leap-frog is self-starting since the positions are now known $\Delta t/2$ ahead of the velocities. To summarize, Eq. (3) is used just once in order to obtain the starting values v^0 and $r^{\Delta t/2}$. The leap-frog integrator, Eq. (2), is then used for all subsequent times, $t=\Delta t, 2\Delta t, 3\Delta t, \ldots$.

2.5. Monte-Carlo ion neutral collisions

Elastic collisions between the ions and a neutral bath gas are included by the Monte-Carlo method. The implementation of MC collisions in our codes is similar to that described by Londry et al., except that we include hard sphere collisions, as well as Langevin collisions [1]. Both Langevin and hard sphere collisions are included since the former and latter are most important at low and high relative velocities, respectively. The MC algorithm assumes that each simulation particle (which represents many individual ions), as far as ion neutral collisions are concerned, behaves as a single ion. The algorithm begins by determining whether a particle has a collision with a neutral atom of the bath gas. For each particle, a neutral atom velocity vector is chosen randomly from the Maxwell-Boltzmann distribution. For a collision cross-section σ (which is the sum of the hard sphere and Langevin cross-sections), neutral gas density n_g, and relative velocity between particle and neutral atom v_r, the probability that a collision occurs is given by [16]

$$P_c=1-\exp(-n_g\sigma v_r\Delta t) \qquad (4)$$

which is accurate if Δt is small enough that $P_c \ll 1$. A random number R, uniform between 0 and 1, is chosen. If $P_c>R$, then a collision occurs, in which case the particle's velocity vector in the center of mass frame is given a random direction, then transformed back to the laboratory frame as described by Londry et al. [1]. The particle position r remains unchanged immediately after the collision. Only the velocity v is affected as a result of the elastic collision. In

---

order to speed up
atom velocity vec
every time the M
three calls to a
other coding. In
simulation an a
velocity vectors is
mann distributio
neutral velocities
pre-calculated set
While the MC
to elastic ion-neu
MC method is e
collision process
exchange, ionizat
cal cross-sections
PIC and MC coll
late entire exper
volving simultane
neutral scatterin
and various chem

3. Results and di

Below, the two
plied to a numbe
to trapped ions. I
an axisymmetric
cal trap with a c
along the trap's
results are ident
from full three-c
physical systems
drically symmet
charge distributi
code is applied
clouds moving in
the merger of t
Helmholtz instab
tions, and image
cyclotron motio
propriate experin
are available, w
tions yield predic
with experiment

3.1. Simulation re

The cylindric
(rzPIC) assumes

order to speed up the MC calculation, the neutral atom velocity vector is not created from scratch every time the MC algorithm is called, requiring three calls to a random number generator and other coding. Instead, at the beginning of the simulation an array of 10 000 random neutral velocity vectors is stored from the Maxwell-Boltzmann distribution. During the simulation, the neutral velocities are chosen randomly from this pre-calculated set.

While the MC algorithm is currently restricted to elastic ion-neutral collisions in our codes, the MC method is easily generalized to any known collision process (e.g. inelastic collisions, charge exchange, ionization) given empirical or theoretical cross-sections [16]. With the combination of PIC and MC collisions one can conceivably simulate entire experimental sequences perhaps involving simultaneously ions, electron beam, ion-neutral scattering, ionization, charge exchange and various chemical reactions.

3. Results and discussion

Below, the two dimensional PIC codes are applied to a number of problems which are relevant to trapped ions. First, *rz*PIC is employed to study an axisymmetric ion cloud confined in a cylindrical trap with a constant magnetic field directed along the trap's *z*-axis. The *rz*PIC simulation results are identical to what one would obtain from full three-dimensional simulations for the physical systems considered below; namely, cylindrically symmetric confinement geometry and charge distribution. Next, the Cartesian *xy*PIC code is applied to the dynamics of off-axis ion clouds moving in the *xy* plane under $E \times B$ drift, the merger of two off-axis ion clouds, Kelvin-Helmholtz instability in hollow charge distributions, and image charge detection of coherent cyclotron motion. In all situations where appropriate experimental data or analytical models are available, we demonstrate that the simulations yield predictions which agree quantitatively with experiment and analytical theory.

3.1. Simulation results employing rzPIC

The cylindrical particle-in-cell simulator (*rz*PIC) assumes that the device and charge distribution have cylindrical symmetry. In this case the simulation results from *rz*PIC are identical to full three dimensional simulations by symmetry. Therefore, *rz*PIC may reliably be applied to such problems as charged beams in cylindrical ion optical devices; ellipsoidal ion clouds aligned along the trap symmetry axis of an rf Paul, Penning or cylindrical trap; on-axis ion injection into one of these cylindrically symmetric traps; or an axially symmetric ion source. Below, *rz*PIC is used to study the maximum number of ions which can be confined in a cylindrical ICR trap, including experimental parameter dependencies, and the cooling of an ion cloud in a combined trap by ion-neutral collisions.

3.1.1. Maximum ion population and equilibrium cloud shape

The first application presented is to determine the maximum number of ions which can be confined in an ICR trap. A cylindrical ICR trap (5 cm diameter and 5 cm length) is allowed to fill to capacity with ions by introducing particles over many time steps at a constant current at random positions within a 1-mm radius cylindrical volume which extends the entire trap length. Neglecting space charge effects, there is no limit to the number of particles which can be confined. However, the space charge potential limits the maximum total charge and number density which can be confined. These are actually two different limits. The maximum charge which can be confined is determined by the condition that the space charge potential just equals the trapping well depth [33,39]. This is called the *z*-confinement limit since the well depth is calculated along the trap's *z*-axis. The second limit is determined by the radial force balance condition that an ion is confined only if the radially inward magnetic force is greater than the sum of the outward centrifugal and space charge forces [34,39,42]. This condition defines a maximum number density which can be confined known as the Brillouin density limit ($n_B = \varepsilon_0 B^2/2m$).

Fig. 3 shows equilibrium particle configurations at $B = 1$ T for three different potentials applied to the end caps with ground on the ring electrode. These equilibria are reached by introducing as many particles as the trap can hold. Subsequently, no additional particles are introduced into the trap and the particles are followed for another 4000 time steps. We find that the maximum number of ions which can be confined is proportional to the trap potential in qualitative agreement with a simple analytical model. A simple model for the z-confinement limit, based on the assumption that the ion cloud is a uniform density cylinder of charge, predicts that the maximum number of ions (charge q) contained in an ion cloud (cloud radius ρ_c and length L) is [33,39]

$$N_{\max} = \frac{4\pi\varepsilon_0 L V_d}{q}\left(1 + 2\ln\frac{r_w}{\rho_c}\right)^{-1} \qquad (5)$$

where r_w is the radius of the confinement geometry and V_d is the trap potential well depth in volts. Eq. (5) agrees surprisingly well with the maximum number of ions confined in an actual cylindrical trap by the PIC simulations. The dependence on r_w is due to the image charge. The trapping well depth V_d is the difference between the potential at the end caps and the potential at the trap center when the trap is space charge free. For a cylindrical trap whose length and diameter are equal with a potential difference of V_t between endcap and ring electrode, $V_d \cong 0.72\ V_t$. Putting this in Eq. (5) yields a maximum number of ions which can be confined equal to $3.3 \times 10^6\ V_t$ which compares well with the numerical simulations which find maximum numbers of singly charged ions equal to 0.26×10^6, 2.6×10^6, and 36.0×10^6 at trapping voltages (V_t) equal to 0.1, 1.0 and 10.0 V, respectively.

While the equilibrium configuration for a full trap with $V_t = 0.1$ V and $V_t = 1.0$ V is approximately cigar-shaped and 1-mm radius, it is evident that for $V_t = 10$ V the ion cloud radius is considerably greater than 1 mm. The reason for this expansion is that the Brillouin density limit ($n_B = 2.66 \times 10^{13}$ m^{-3}) is reached before the z-confinement limit is reached in Fig. 3c. If an ion cloud reaches its Brillouin limit before the z-confinement limit is reached, the ion cloud expands radially such that its number density is below the Brillouin limit. The measured number densities at the ion cloud centers (averaged over a small volume within the ion cloud) for a full trap from the simulations at $V_t = 0.10$, 1.0 and 10.0 V are 0.12×10^{13}, 1.0×10^{13}, and 2.4×10^{13} m^{-3}, respectively, with an uncertainty of approximately ±15%. The number density for the simulation run with $V_t = 10.0$ V is close to the Brillouin limit. It is actually possible for the ion cloud to contact the ring electrode before the z-confinement limit is reached if the trap potential and magnetic field are sufficiently high and low, respectively. One should note from Eq. (5) that the z-confinement limit is independent of magnetic field. Additional simulations carried out at 2 T gave nearly identical maximum total charge which can be confined as the 1 T simulations. However, since the Brillouin number density limit is proportional to B^2/m and independent of charge, higher magnetic fields may be required if a large population of high molecular mass ions is to be confined in a small volume.

It is interesting to look at the total potential (trap + space charge + image charge) along the z-axis as the trap fills to capacity with ions. Fig. 4 plots the electric potential along the z-axis for five different numbers of ions, ranging from zero (empty trap) to 2.6×10^6 singly charged ions (full trap) modeled by 25 000 simulation particles, when the end caps are at 1 V. At $V_t = 1$ V, $m = 100$ u and $B = 1$ T, the Brillouin limit is not surpassed for a 0.1-cm radius cylindrical ion cloud, even when the trap is completely filled with ions (i.e. the ion cloud does not radially expand appreciably beyond the initial 0.1-cm cloud radius as observed in Fig. 3b). As the trap fills with ions, the potential flattens in the trap center. Qualitatively, the space charge shields the trap electric field along the z-axis, modifying the potential from quadrupolar to particle-in-a-box. At high ion populations and low trap potentials, the ions arrange themselves in such a way that the space charge potential negates the applied trap potential, resulting in particle-in-a-box behavior along the z-axis. The assumption of a quadrupolar potential is incorrect even for 0.15×10^6 ions with these conditions. As the ion population increases, the well depth decreases until the space charge potential completely negates the trap potential. For end cap potentials other than 1 V, these curves are basically the same as in Fig. 4, except

Fig. 3. Equilibrium
different trap potenti
confined: (a) $V_t = 0.1$
A 1-T magnetic field
respectively. The ma
m/z 100 are injected
cm and length 5 cm
50 × 100 cells.

10.0 V are
^{13} m^{-3}, re-
proximately
simulation
llouin limit.
d to contact
ement limit
gnetic field
tively. One
onfinement
Additional
arly identi-
e confined
e the Bril-
ortional to
igher mag-
population
nfined in a

l potential
along the
ions. Fig. 4
z-axis for
from zero
d ions (full
icles, when
m = 100 u
surpassed
oud, even
ions (i.e.
apprecia-
radius as
with ions,
. Qualita-
ip electric
potential
At high
, the ions
the space
ap poten-
ior along
polar po-
ions with
increases,
e charge
potential.
V, these
4, except

the number of ions is scaled by the trap potential. For example, if $V_t = 0.1$ V with all other parameters remaining the same, the curve corresponding to 0.15×10^6 ions for 1 V is the same as 0.15×10^5 ions for 0.1 V.

3.1.2. Combined trap with collisional cooling

A more complicated application of the code *rz*PIC is to study the evolution of an ion cloud in a combined trap (i.e. a Paul trap in a constant magnetic field) with the addition of a high neutral background pressure [40]. The cylindrical trap has the same dimensions as above (5 cm length and 5 cm diameter). An rf-only potential (1 MHz; 5000 $V_{0\text{-p}}$) is applied to the ring electrode with ground on the end caps ($V_t = 0$ V). The trap is in a 1-T magnetic field with a bath gas of 50 mtorr N_2 in thermal equilibrium at 300 K temperature. The ion cloud, composed of m/z 1000 ions, is initially cigar-shaped with cloud radius 0.1 cm extending the entire trap length.

In order to discern the relative importance of space charge effects on the cloud shape, we compare two different simulation runs. In the first case, Coulomb interactions are neglected altogether, while in the second run, space charge effects between 4.4×10^6 singly charged m/z 1000 ions modeled as 2000 particles in the PIC simulation are self-consistently followed in time. If Coulomb interactions are negligible, the ion cloud cools to a small volume at the trap center determined by the pseudopotential, the ion-neutral mass ratio, and the neutral gas temperature. From Fig. 5a the equilibrium distribution is nearly spherical in shape and of relatively small spatial extent when Coulomb interactions are neglected. On the other hand, Fig. 5b demonstrates that for 4.4×10^6 e charge and the other conditions used in the simulation, the ion cloud actually expands radially. The equilibrium shape is actually an

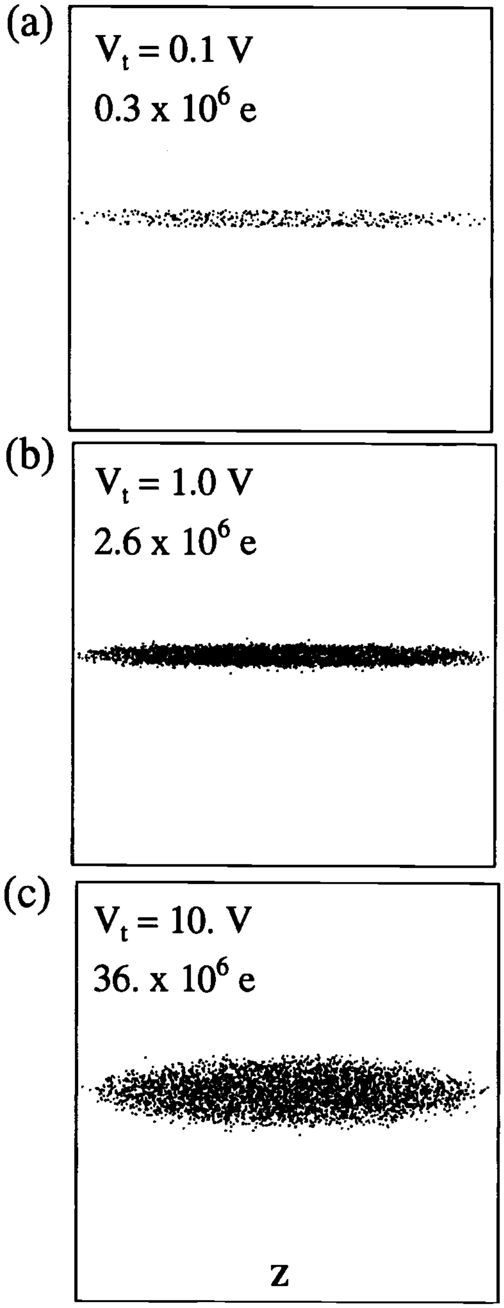

Fig. 3. Equilibrium particle configurations in the *xz* plane for a cylindrical ICR trap filled to capacity with space charge. Three different trap potentials are used corresponding to three different maximum numbers of singly charged m/z 100 ions which can be confined: (a) $V_t = 0.1$ V and 0.3×10^6 singly charged ions; (b) $V_t = 1.0$ V and 2.6×10^6 ions; and (c) $V_t = 10.0$ V and 36.0×10^6 ions. A 1-T magnetic field is applied parallel to the trap *z*-axis. Potentials V_t and ground are applied to the end caps and ring electrode, respectively. The maximum charge which can be confined is approximately proportional to trap potential well depth. Particles with m/z 100 are injected over many time steps in a cylindrical volume with radius $\rho_c = 0.1$ cm and length 5 cm until the trap (radius 2.5 cm and length 5 cm) cannot hold additional particles. The simulation time step is 0.65 μs and the computational *rz* mesh is 50×100 cells.

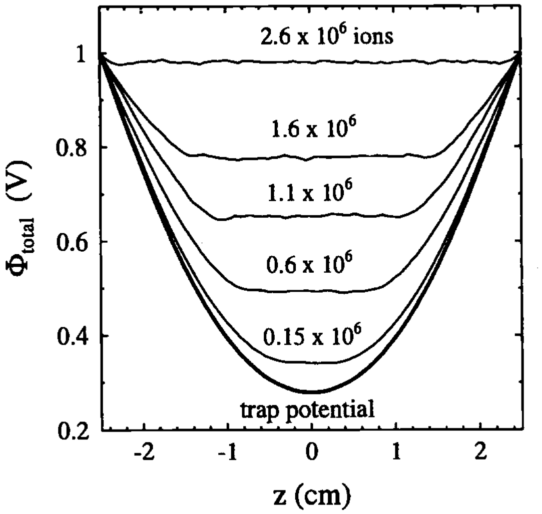

Fig. 4. The total electrostatic potential along the *z*-axis for different numbers of singly charged m/z 100 ions confined in a cylindrical trap (trap potential 1 V, radius 2.5 cm, length 5 cm). The total number of ions range from an empty trap to a completely filled trap containing 2.6×10^6 ions. Parameters include 25×10^3 simulation particles, 1-T magnetic field and 0.65-μs time step. Particles are initially injected into the cylindrical ICR trap within a radius of 0.1 cm from the *z*-axis, then are allowed to equilibrate over many time steps.

oblate ellipsoid for these conditions with the major axis four times longer than the minor axis. This shape follows a contour of constant pseudopotential, and represents a force balance between the space charge potential and applied pseudopotential. The maximum density of this distribution is $\sim 1.5 \times 10^7$ cm^{-3} which is close to a theoretical estimate of 1.3×10^7 cm^{-3}, where the latter is based on the assumptions that the maximum density occurs when the space charge potential just equals the pseudopotential well depth and that image charge effects are negligible [41]. Collisionally cooled ions in a combined trap with a deep pseudopotential well are focused towards the well minimum. However, eventually the Coulomb repulsion between ions prevents all of the ions from reaching the center. The equilibrium configuration is reached when the space charge potential equals the pseudopotential with the cloud boundary coincident with a pseudopotential contour.

3.2. Simulation results employing xyPIC

The Cartesian PIC code (*xy*PIC) treats the *z*-variable as ignorable, meaning that there is no *z*-dependence for the fields. The particles are, therefore, infinitely long charged rods aligned parallel to the *z*-axis. The *xy*PIC code is used to study basic aspects of ion cloud dynamics in the *xy* plane of an ICR trap. Though not done here, it is easy to modify the *xy*PIC code to study ion behavior parallel to the applied magnetic field by directing the magnetic field along either the *x* or *y* axis [21].

The first problem we address is the effect of ion-neutral collisions on an initially cold uniform density ion cloud whose symmetry axis coincides with the trap geometric center. In these simulations a 1-T magnetic field is directed parallel to the *z*-axis. Furthermore, the trap radial boundary is at ground potential. This is not a restriction in our codes, but rather a choice of convenience (e.g. each electrode point may take on a different potential). An initial ensemble of 5×10^4 simulation particles is distributed within a radius of 0.3 cm from the trap center by a uniform random number generator. The particle charge per length is chosen to model 1×10^6 singly charged ions in a 5-cm long trap. The initial number density within this ion cloud is $n_0 \approx 7.1 \times 10^5$ cm^{-3}. This density is much lower than the Brillouin maximum density limit of $n_B \approx 1.8 \times 10^7$ cm^{-3}, thereby guaranteeing good radial confinement for this cloud. In the simulations, the m/z 150 particles are allowed to interact via their Coulomb interaction as well as with a 1.5 mtorr He collision gas which has a 300-K Maxwell-Boltzmann distribution. The configuration is followed in time to determine the effect of the bath gas on the particle distribution.

Fig. 6a plots the ion speed distribution at three different times in the simulation, corresponding to different average numbers of ion-neutral collisions per ion. The broken line in Fig. 6a is the theoretical 300-K Maxwell-Boltzmann speed distribution without any fitted parameters. While initially all ions start at rest in the simulation, their speed distribution closely approaches

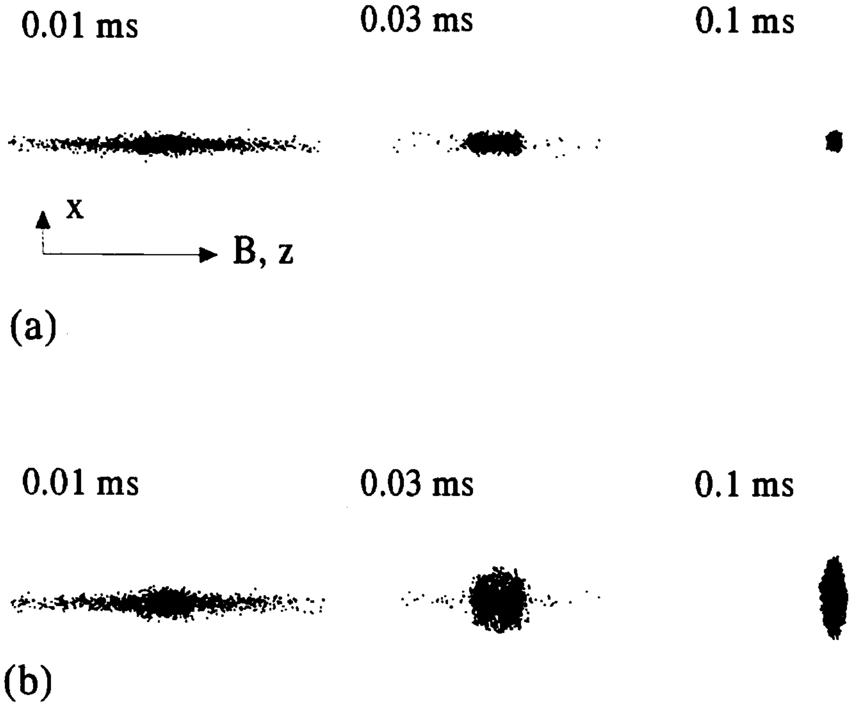

Fig. 5. Relaxation of an initially cigar-shaped ion cloud ($\rho_c = 0.1$ cm) by thermalizing 300-K ion-neutral collisions in a cylindrical trap (radius 2.5 cm, length 5 cm) operating in the combined trap mode. A 1-MHz rf potential with $V_{0\text{-p}} = 5000$ V is applied to the ring electrode with zero potential on the end caps. In (a) Coulomb interactions between particles are neglected while in (b) the total charge is 4.4×10^6 e. Other parameters include 50 mtorr N_2 bath gas, $B = 1$ T, 2000 simulation particles, $q = e$, m/z 1000, 50×100 computational mesh and 0.033-μs time step.

Maxwellian after each particle undergoes > 100 ion-neutral collisions. The ions clearly reach a thermal equilibrium with the bath gas after ~ 100 collisions/ion. The good agreement between the computer simulation result and the theoretical distribution attests to the ability of the Monte-Carlo method to accurately simulate ion-neutral collisions. This observation suggests that a simple procedure to generate a thermal equilibrium distribution of ions is simply to start the simulation with some non-thermal distribution then introduce a collision gas just long enough to achieve thermal equilibrium.

The radial dependence of the number density is shown in Fig. 6b for two different times in the simulation run, corresponding to two different average number of collisions per ion. Initially, the particles are in a top hat distribution where the density is n_0 within the cloud then falls abruptly to zero for radii greater than 0.3 cm, the ion cloud radius. As the number of collisions increases, the central density decreases and the cloud expands radially. A non-zero temperature has a Gaussian radial dependence which is identical to a Maxwell-Boltzmann distribution in the frame of reference rotating with the cloud's $E \times B$ drift [42]. Most of this expansion is related to a negative energy effect analogous to magnetron mode expansion. The space charge electric field within the ion cloud is directed radially outward. This radial electric field results in an $E \times B$ rotation of the ion cloud about the cloud's symmetry axis, which happens to coincide with the trap z-axis in this simulation. The radial outward electric field is defocusing. Ion-neutral collisions radially expand the ion cloud. However, radial expansion slows with time (remember that there are no applied trap fields) since the space charge radial electric field is proportional to the density, which decreases as the cloud expands.

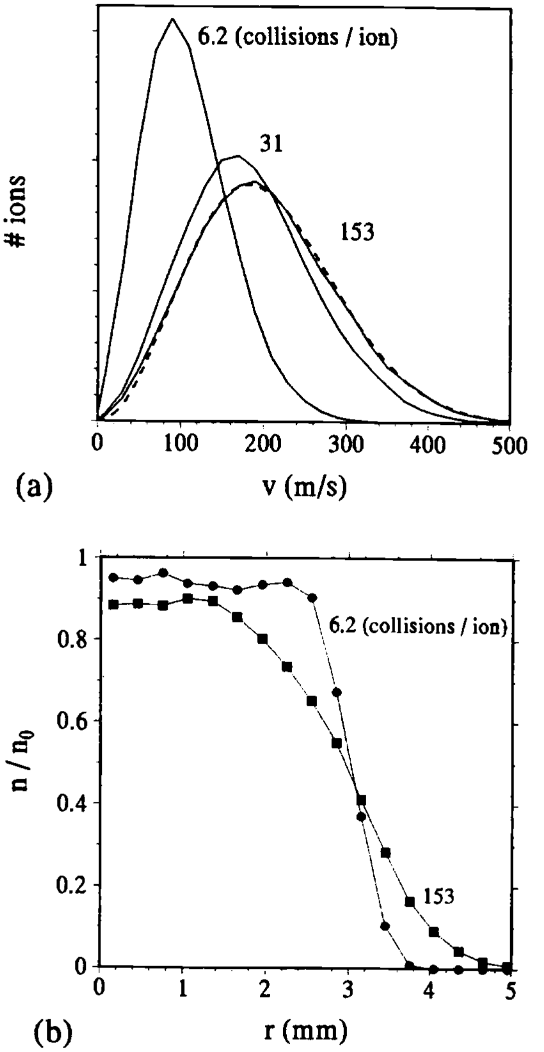

Fig. 6. Thermalization of an on-axis initially cold m/z 150 ion cloud by ion-neutral collisions with 1.5 mtorr He bath gas at 300 K temperature. The 0.3-cm radius ion cloud consists of 5×10^4 simulation particles (m/z 150) whose total charge is set to model a system of 1×10^6 singly charged m/z 150 ions. Different average numbers of collisions per ion, corresponding to different times during the simulation run, are indicated; (a) plots the ion speed distribution showing close agreement with the theoretical 300 K Maxwell-Boltzmann distribution (broken line) at 153 collisions/ion, while (b) shows the radial density profile normalized to the initial density at different numbers of collisions per ion. The *xy*PIC code is used in this and subsequent simulations. Parameters include a 128×128 *xy* computational mesh with ground on the *xy* electrode boundaries, a 1-T magnetic field directed along the *z*-axis and a 1.9-μs time step.

3.2.1. Dynamics of an off-axis charge column with circular cross-section

In this simulation the ion cloud (a column of charge) is displaced from the trap symmetry axis in effect giving the ion cloud a coherent magnetron mode. If one neglects Coulomb effects, the ion cloud does not move in time since there is no applied trap potential to produce a radial electric field. The presence of Coulomb interactions in actual systems causes the ion cloud to rotate about its own symmetry axis due to the internal space charge $E \times B$ drift and to rotate the ion cloud as a whole about the trap's own symmetry axis due to image charge-induced $E \times B$ drift.

Fig. 7 depicts the evolution of an off-axis ion cloud moving under the influence of its own image charge induced on the electrodes and internal Coulomb electric field. The ion cloud has an initial constant density of 7.1×10^5 cm^{-3} and models a 0.3-cm radius ion cloud consisting of 1×10^6 singly charged m/z 150 ions. The ion cloud is initially positioned 1.5 cm from the center of a 5-cm wide grounded trap whose cross-section is either (a) square or (b) circular. Particle positions are plotted at four different discrete times. In addition, Fig. 7 shows the complete trajectory (50 ms) of a single representative particle (broken line) and the ion cloud center of mass position (solid line). The two most important dynamical effects observed are a relatively fast internal cloud rotation and a slow rotation of the entire cloud around the trap *z*-axis.

The image charge is present since the trap boundary is an equipotential. The interaction between the image charge induced on the trap boundary with the ion cloud gives rise to an electric field directed radially outward from the trap geometric center through the ion cloud center of mass. The resulting image charge-induced $E \times B$ drift is a rotation about the trap center. The rotation frequencies are ≈ 19 Hz and ≈ 23 Hz for the square and circular traps, respectively. This measured image charge-induced rotation frequency for the cylindrical trap is identical to the result obtained from an analytical model

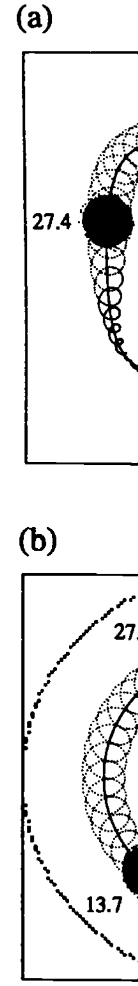

Fig. 7. The dynamics
1.5 cm from the *z*-axis
and (b) a trap with a
points are at zero pot
the entire cloud at fou
ion cloud center of m
representative particle
tion. In (b) the capacit
the cylindrical bounda
tially uniform and the
5000 simulation partic
tional mesh with grou
magnetic field directed
The ion cloud, consisti
m/z 150 and charge 2
1×10^6 singly charged

which assumes th
[30]. These freque

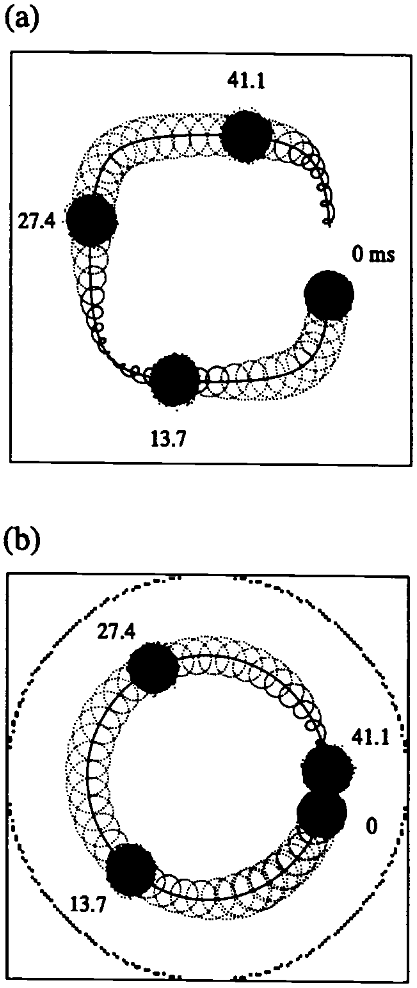

Fig. 7. The dynamics of a 0.3-cm radius ion cloud displaced 1.5 cm from the z-axis of (a) a trap with a square cross-section and (b) a trap with a cylindrical cross-section. The electrode points are at zero potential. Particle positions are plotted for the entire cloud at four discrete times. Also indicated are the ion cloud center of mass position and trajectory for a single representative particle at all times during the 50 ms simulation. In (b) the capacitance matrix method is used to maintain the cylindrical boundary condition. The cloud density is initially uniform and the ions start at rest. Parameters include 5000 simulation particles, m/z 150, a 128×128 xy computational mesh with ground on the xy electrode boundaries, a 1-T magnetic field directed along the z-axis and a 1.9-μs time step. The ion cloud, consisting of 5000 simulation particles, each of m/z 150 and charge 200 e, models an ion cloud composed of 1×10^6 singly charged ions.

which assumes that the ion cloud is a line charge [30]. These frequencies are comparable in magnitude to single ion magnetron frequencies, indicating that efforts aimed at eliminating magnetron motion in ICR traps are only meaningful when space charge effects are negligible since image charge-induced rotation is analogous to magnetron motion. The image charge-induced rotation is faster in the trap with circular cross-section (5 cm trap diameter) compared to the square cross-section trap (5 cm width) owing to a smaller time-averaged ion cloud-electrode wall separation distance for the cylindrical wave guide. The center of mass trajectories are also different for the two wave guides. The ion cloud in a cylindrical wave guide follows a circular trajectory with a constant speed while in a square wave guide the trajectory is box-shaped, owing again to the $E \times B$ drift which indicates that the cloud trajectory follows an equipotential. In contrast to the cylindrical trap, the center of mass speed for an off-axis ion cloud in a trap with a rectangular boundary is not constant. In Fig. 7a for the square wave guide, the ion cloud center of mass moves faster the closer the cloud is to an electrode wall resulting in a non-uniform speed over the trajectory (i.e. the cloud is slowest at the trap corners).

A more pronounced and ubiquitous dynamical effect is the internal $E \times B$ rotation arising from the ion cloud's own internal Coulomb electric field. This rotation is observed in Fig. 7 for one of the particles within the ion cloud as the spiral curve about the center of mass trajectory. The internal $E \times B$ rotational frequency, ω_r, is approximately (2π) 1.0 kHz for both Fig. 7a and b, estimated by just counting the oscillation periods a single particle within the ion cloud undergoes during the 50 ms detection time. This frequency is directly comparable to an analytical estimate based on the assumptions that the density is constant and that the image charge has a negligible effect on the internal cloud dynamics. The internal $E \times B$ rotation frequency ω_r for an infinitely long cylindrical cloud of uniform density is [11]

$$\omega_r = \frac{nq}{2\varepsilon_0 B} \tag{6}$$

With $n = 7.1 \times 10^{11}$ m^{-3}, $q = e$ and $B = 1$ T, the theoretical $\omega_r = (2\pi)$ 1.02 kHz which is in very good agreement with the *xy*PIC simulation result based on the trajectory of a single particle within the ion cloud. A more general formula which is valid for all constant density ellipsoidal ion clouds, not just rod-shaped, has been reported previously [43].

Thus far, the off-axis ion cloud represents a zero temperature equilibrium since all particles start from rest and the density is uniform across the cloud. Finite Larmor radius effects are now included by first thermalizing the ion cloud with 1.5 mtorr He collision gas, which has a 300-K Maxwell-Boltzmann distribution, for 2 ms. This collision time and pressure are sufficient to give an average of ~ 100 collisions/ion. Subsequently, the bath gas is removed and the particles followed for a relatively long detection period. Fig. 8 plots particle positions for the thermalized off-axis ion cloud. The remaining simulation parameters are identical to those given in Fig. 7a for the square trap. While the ion cloud appears diffuse due to the Gaussian density profile, there is no noticeable difference between the center of mass trajectories for 300 K (Fig. 8a) and 0 K (Fig. 7a). However, there are differences in the dynamics of individual particles within the cloud. This is evident in Fig. 8b which plots the trajectory of a single particle within the 300 K off-axis ion cloud, showing the finite cyclotron motion in addition to the internal $E \times B$ rotation. The internal rotation frequency for this particle is ~ 0.9 kHz, somewhat less than the ~ 1.0 kHz observed for the 0 K case described above. This reduction in frequency is attributable to a commensurate reduction in number density as a result of ion-neutral collisions. The trajectory plotted in Fig. 8b is for a particle in the high velocity tail of the Maxwell-Boltzmann distribution, resulting in an observable cyclotron orbit superimposed on the larger orbital radius internal $E \times B$ rotation. Three general motions are observed in Fig. 8b for an individual ion within the ion cloud: the relatively slow image charge-induced $E \times B$ drift around the trap geometric center; the internal ion cloud $E \times B$ drift; and the fast cyclotron motion.

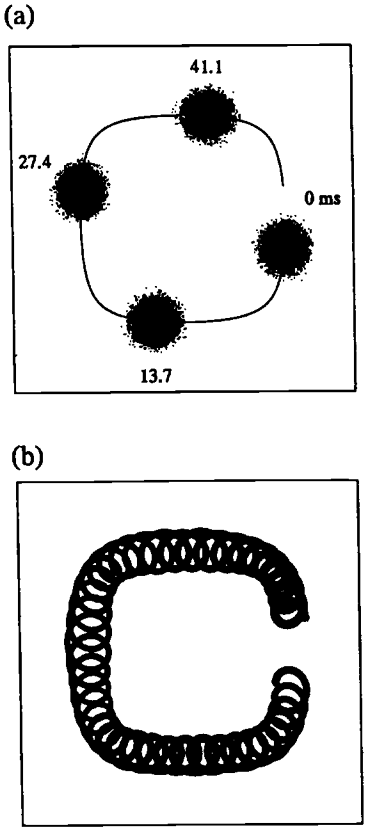

Fig. 8. Dynamics of an off-axis thermal 300-K ion cloud in a square wave guide. (a) Particle positions and center of mass trajectory. (b) The trajectory of a single representative particle chosen from the distribution. The thermal equilibrium is achieved by allowing the initially cold ions to undergo ~ 100 collisions/ion with a 1.5 mtorr He bath gas for 2 ms. Subsequently, the bath gas is removed and the particles followed for an additional 50 ms. The other simulation parameters are identical to those in Fig. 7a.

Space charge-induced internal ion cloud rotation is an ubiquitous phenomenon present in practically every FT-ICR experiment. The internal cloud rotation is of fundamental importance to understanding charge particle confinement, stability of coherent modes, and mode locking [11,25,33,43]. Stability enhancement owing to the internal ion cloud Coulomb $E \times B$ drift may be an important reason why FT-ICR mass spectrometers achieve ultrahigh resolution [43].

3.2.2. Merger of two off-axis charge columns

There is an exact analogy between the equations of motion governing the two dimensional

$E \times B$ drift and two dimensional fluid dynamics. The 2D (xy) $E \times B$ drift dynamics are isomorphic to the 2D Euler equations for an incompressible inviscid fluid [24–27,31]. The fluid analogy is that charge density is proportional to fluid vorticity. Hence, surface charge perturbations on charged columns, called diocotron modes, are equivalent to surface ripples on extended fluid vortices [24]. This is an important problem since, for example, planetary atmospheres are approximately near inviscid (high Reynold's number) 2D fluid flows. The previous simulations on a single off-axis charge column are equivalent to the dynamics of a fluid vortex. The most famous example of a long-lived near inviscid vortex in nature is probably Jupiter's red spot. The 2D Euler equations are of intense current interest since this dynamical system exhibits turbulent flow for many initial distributions [27].

The fluid analogy implies that the 2D drift dynamics for two off-axis charged columns are equivalent to the dynamics of two extended fluid vortices. An amazing result, which is verified by electron plasma experiments, is that if the ion clouds are sufficiently close they will merge into a single charge distribution [25]. Fluid calculations and experiment show that vortex merger takes place if the initial distance between two off-axis charge columns is less than about 1.6 times their diameter [25]. Since this is a quantitative result for a very interesting dynamical system, we have simulated the dynamics of two off-axis ion clouds for different initial separation distances as a partial test of the accuracy of the xyPIC code.

Two identical charge columns are initially separated from each other by displacing each column an equal distance from the trap center along the x-axis. The two charge columns are each 0.3 cm in radius with initial separation distances between their centers ranging from 0.9 cm and 1.14 cm, corresponding to initial separation distances ranging from 1.5 and 1.9 times the diameter of one of the charge columns. There are 5000 particles with m/z 100 and $q = e$ in each charge column. The initial number density is 3.5×10^5 cm^{-3}. The particle trajectories are followed through time. Fig. 9 and Fig. 10 show particle positions at different times for three different initial separation distances.

Fig. 9 shows snapshots of particle positions at different times when the initial separation distance between cloud centers is 1.5 times the diameter of one cloud. This simulation clearly shows vortex merger. On the other hand, in Fig. 10a and b the initial separation distances between cloud are 1.7 and 1.9 times the cloud diameter, respectively. The vortices (charged rods) do not merge into a single vortex for these latter cases, but instead rotate around each other. These simulations are in agreement with experimental data on two extended charge columns confined in a Penning-Malmberg trap [25].

From Fig. 9, if the two vortices are closer than the critical separation distance of about 1.6 times the column diameter, then merger occurs on a time scale on the order of approximately one-half of a revolution period of the two columns owing to their $E \times B$ drift. An estimate of the revolution period for two charge columns (neglecting image charge), each with radius ρ_c, separated by a distance s is

$$\tau \approx \frac{8\pi\varepsilon_0 B}{nq}\left(\frac{s}{2\rho_c}\right)^2 \tag{7}$$

With $n = 3.5 \times 10^{11}$ m^{-3}, $B = 1$ T, $q = e$, and $s/2\rho_c = 1.5$, corresponding to the conditions in Fig. 9, the time-scale for merger to occur based on Eq. (7) is approximately $\tau/2 = 9$ ms, in order of magnitude agreement with the simulation.

3.2.3. Kelvin-Helmholtz instability in a hollow beam

This section describes a series of computer experiments on hollow beam distributions. A hollow beam ion cloud is a hollow cylinder of charge whose cross-section in the xy plane is ring-shaped. These hollow distributions exhibit very interesting dynamics, most notably the Kelvin-Helmholtz instability [26]. This instability arises due to the unfavorable velocity shear across the hollow cylinder distribution. In non-neutral plasma experiments employing Penning-Malmberg traps this distribution is created, for example, by grounding one of the end cap potentials for a

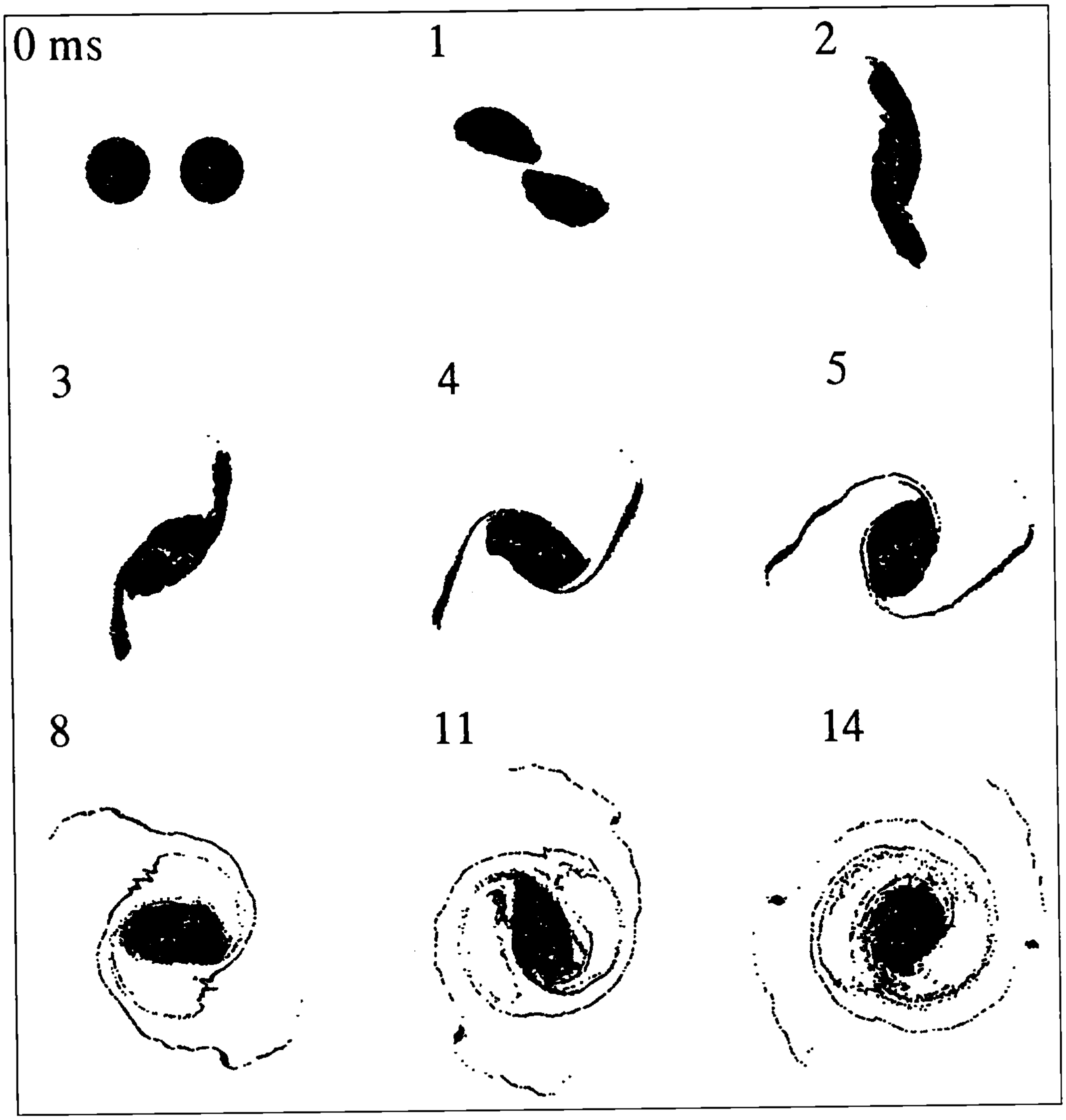

Fig. 9. Vortex merger in two off-axis charge columns. Particle positions at nine different times in the simulation run are plotted. The initial separation distance between column centers equals 1.5 times the diameter of one column. Parameters include: $\rho_c = 0.3$ cm, 10^4 simulation particles, 128 × 128 mesh, m/z 100, $B = 1$ T, and an initial number density of 3.5×10^5 cm^{-3}. The confinement geometry has a width equal to 5 cm.

short time. Hollow beam distributions are unstable, evolving into a number of vortices due to Kelvin-Helmholtz instabilities (also called diocotron instabilities) [26]. Usually, these vortices evolve through a succession of vortex mergers towards an axially symmetric equilibrium. For other initial distributions, several of the resulting vortices may be exceptionally long-lived, moving chaotically about a non-uniform background vorticity. Under certain circumstances, a new metastable fluid equilibria, called a vortex crystal, has been observed in experiments [27].

The ring ion clouds used in our simulations consist of 10^4 particles and an initial number density of 7.1×10^5 cm^{-3}. The m/z 100 particles are confined by a 2.5-cm radius grounded cylinder

---

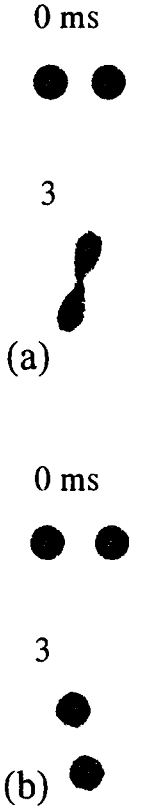

Fig. 10. Dynamics o
separation distances
diameter of one cha
same as in Fig. 9.

aligned parallel t
radius of the ini
simulations whil
different simulat
geometry is cylin
cle interactions c
canonical angula
a conserved qua
ergy. The canoni
energy are conse
lations.

The first simul
distribution whos
and 0.75 cm, re
positions at nine
The circular bo
2.5-cm radius co

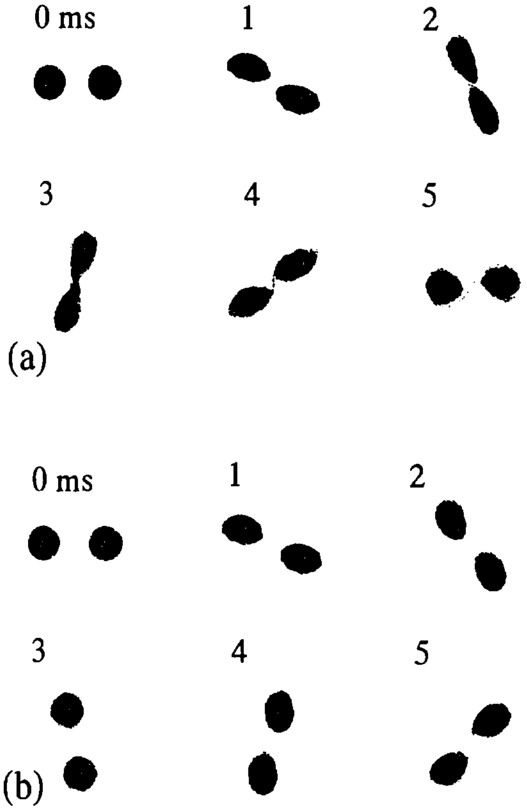

Fig. 10. Dynamics of two off-axis charge columns at initial separation distances equal to (a) 1.7 and (b) 1.9 times the diameter of one charge column. Other parameters are the same as in Fig. 9.

aligned parallel to a 1-T magnetic field. The outer radius of the initial distribution is 1.0 cm in all simulations while the inner radius is varied in different simulation runs. Since the confinement geometry is cylindrically symmetric and like particle interactions conserve angular momentum, the canonical angular momentum about the *z*-axis is a conserved quantity in addition to the total energy. The canonical angular momentum and total energy are conserved to within 0.1% in our simulations.

The first simulation involves an initially hollow distribution whose outer and inner radii are 1.0 and 0.75 cm, respectively. Fig. 11 plots particle positions at nine different times in the simulation. The circular boundary is the boundary of the 2.5-cm radius confinement cylinder maintained at zero potential. This hollow density profile is unstable as already evident by 2 ms into the simulation. At 2 ms the Kelvin-Helmholtz instability, with fastest growing unstable azimuthal mode number equal to five, is evident as the ring breaks into five density clumps. By 22 ms into the simulation, these density clumps (vortices) evolve through a series of vortex mergers into an approximately axially symmetric equilibrium whose density maximum is close to the trap symmetry axis.

The number of vortices which result at the onset of instability depend on the ratio of ring radius divided by the ring thickness [26]. The greater the radius to thickness ratio, the greater the number of resulting vortices. Our simulations are in agreement with this result. Fig. 12 shows the initial onset of instability for four different thickness rings. The outer radius is 1 cm with the ring thickness indicated in the figure. Furthermore, the number of vortices at the onset of instability (this number is equal to the fastest growing unstable azimuthal mode number) are in reasonable agreement with experiment [26]. The simulations predict that the mode number of the fastest growing unstable diocotron mode increases approximately linearly with increasing ring radius to ring thickness ratio. In addition the proportionality constant is in reasonable agreement with experiment [26].

While many initial hollow beam distributions evolve through successive events of vortex merger and turbulent mixing, analogously to Fig. 11, towards a single axially symmetric equilibrium, this is not always the case. We find that for sufficiently thin initial ring distributions that several of the vortices can be exceptionally long-lived. For some initial distributions, the final equilibrium is a vortex crystal state characterized by a small number of vortices superimposed on a near uniform density background [27]. Fig. 13 shows snapshots in the long time-scale dynamics of a hollow beam ion cloud (outer radius 1.0 cm, inner radius 0.85 cm) that leads to a vortex crystal. The final equilibrium state in this simulation is five high density vortices, arranged in a pentagon, superimposed on a lower density background that does not reach the cylinder wall. Both the back-

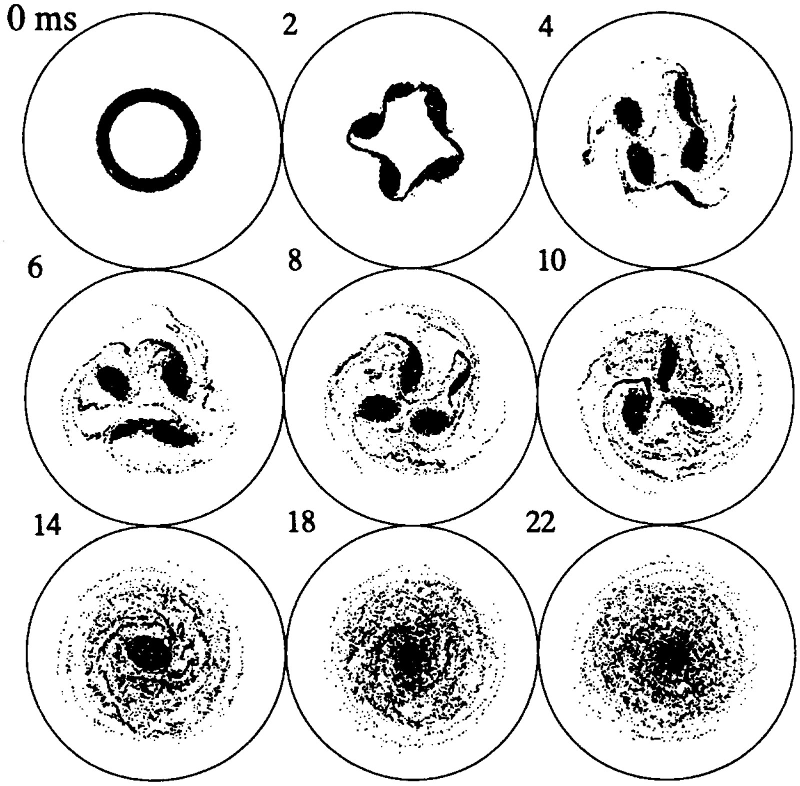

Fig. 11. Particle positions at nine different times in the evolution of a hollow beam ion cloud whose outer and inner radii are 1.0 cm and 0.75 cm, respectively. The circular boundary is the boundary of the grounded confining cylinder whose radius is 2.5 cm. Other parameters include: 10^4 simulation particles, 128×128 mesh, m/z 100, $B = 1$ T, and an initial number density of 7×10^5 cm^{-3}.

ground vorticity and vortices (the higher density regions) are rotating about the trap symmetry axis owing to the $E \times B$ drift. However, in the vortex crystal state the vortices maintain their relative position with respect to each other. Other initial conditions can lead to different final arrangements of higher density regions. Recently, vortex crystals have been observed in non-neutral plasma experiments [27]. Both the experimental data and our simulations have a number of similarities in the vortex crystal state. The vortex crystal is characterized by higher density vortices superimposed on a nearly uniform low density background. Furthermore, the background vorticity does not reach the wall of the confining cylinder. The origin of vortex crystallization is not yet understood, though vortex crystals likely represent a new metastable inviscid fluid state. Since energy is not dissipated in the simulation, indicating that no cooling has occurred, vortex crystals have a different origin than ion or Coulomb crystals [12,21]. It is left to future work to determine the origin and significance of vortex crystallization.

3.2.4. Image charge detection of coherent cyclotron motion

The PIC simulators have, thus far, been applied to ion clouds which have not undergone cyclotron resonance excitation. We present below a simple application of particle-in-cell simulation to coherent cyclotron motion in a single m/z ion cloud. This simulation demonstrates image charge detection and the reliability of the particle simulator *xy*PIC by showing that certain physical properties remain conserved during the detection period. These results serve as a benchmark test to give assurance in the reliability of our codes to make realistic predictions. FT-ICR-MS relies on

---

Fig. 12. Particle posi
outer radius of the in
same as given in Fig.

coherently exciti
ferent m/z ions
ferential charge
no reason why
treated by the p
potential (trap +
correct everywl
geometry, includ
with the PIC me
electrode bound
potential. The in
is directly propo
at the electrod
Gauss's Law resu

$\sigma_s = -\varepsilon_0 E_n$

Since σ_s has uni

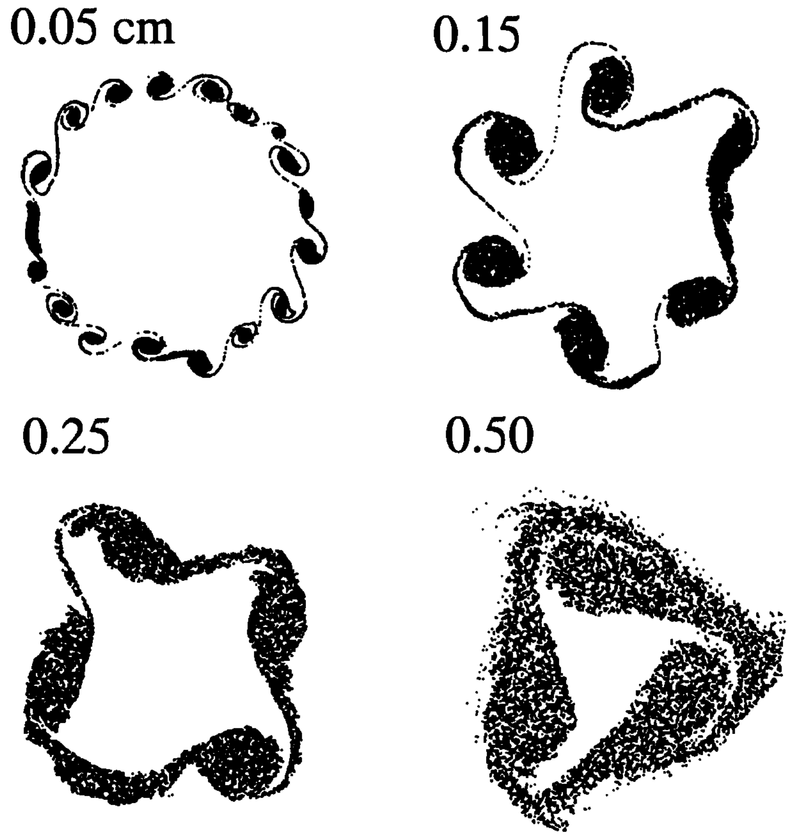

Fig. 12. Particle positions at the onset of Kelvin-Helmholtz instability in four different thickness hollow beam distributions. The outer radius of the initial distribution is 1.0 cm with the ring thickness (0.05, 0.15, 0.25, 0.50 cm) indicated. Other parameters are the same as given in Fig. 11.

coherently exciting the cyclotron modes of different m/z ions, then detecting the induced differential charge on opposing electrodes. There is no reason why cyclotron resonance cannot be treated by the particle-in-cell method. Since the potential (trap + space charge + image charge) is correct everywhere within the confinement geometry, including at the electrode boundaries, with the PIC method, the induced charge on any electrode boundary is directly calculable from the potential. The induced surface charge density σ_s is directly proportional to the normal electric field at the electrode boundary E_n by the simple Gauss's Law result

$$\sigma_s = -\varepsilon_0 E_n \tag{8}$$

Since σ_s has units of charge per area, the induced charge at a particular electrode is computed by integrating σ_s over the electrode surface. For a capacitively dominated detection circuit, the detected voltage transient is equal to the induced charge (at each time step) divided by the circuit capacitance. This method for calculating the induced charge is very accurate since an exact solution to the finite difference form of Poisson's equation is solved at every time step by direct Poisson solvers.

As a partial test of this procedure, a 0.3-cm radius ion cloud containing 1×10^6 e total charge was placed at the center of a 5-cm square trap. Solving Poisson's equation for this system with a 128×128 computational mesh, then calculating the induced charge on all four electrodes by the above procedure yielded a total induced charge equal to the charge contained in the trap to better than 13 significant figures, which is close to machine precision. For all practical purposes, the PIC method for calculating the induced charge is exact.

The direct PIC method for calculating the induced charge more closely approaches the actual experimental procedure for measuring the induced charge than the previously used reciprocity method [28,44]. This is not to imply that there is anything inherently wrong with the reciprocity approach (both procedures should give identical results), just that a computer experiment carried out by the PIC simulation method closely models the major aspects of laboratory-based experiments. The reciprocity method is an elegant and fundamental result in electrostatics that is particularly well adapted to single or few ion simulations. On the other hand, since the total potential is known at all time and space with the PIC simulation method, measuring the induced charge in a PIC computer experiment is very simple. In the reciprocity method, the induced current is calculated from a knowledge of every ion's position (in order to determine the detection electric field associated with that ion) and velocity. Of course, the experiment does not measure the signal this way. During the detection process the experiment measures the induced charge on selected electrodes, regardless of where each individual ion is located or its velocity components. Since the PIC method solves Poisson's equation self-consistently at each time step everywhere within the trap, the induced charge at a particular electrode is directly solved in analogy with the experiment. In particular the PIC method for finding the induced charge only relies on a knowledge of the electric field at the electrode, and not directly on the position and velocity of every particle within the trap.

The particle-in-cell simulator *xy*PIC is used to

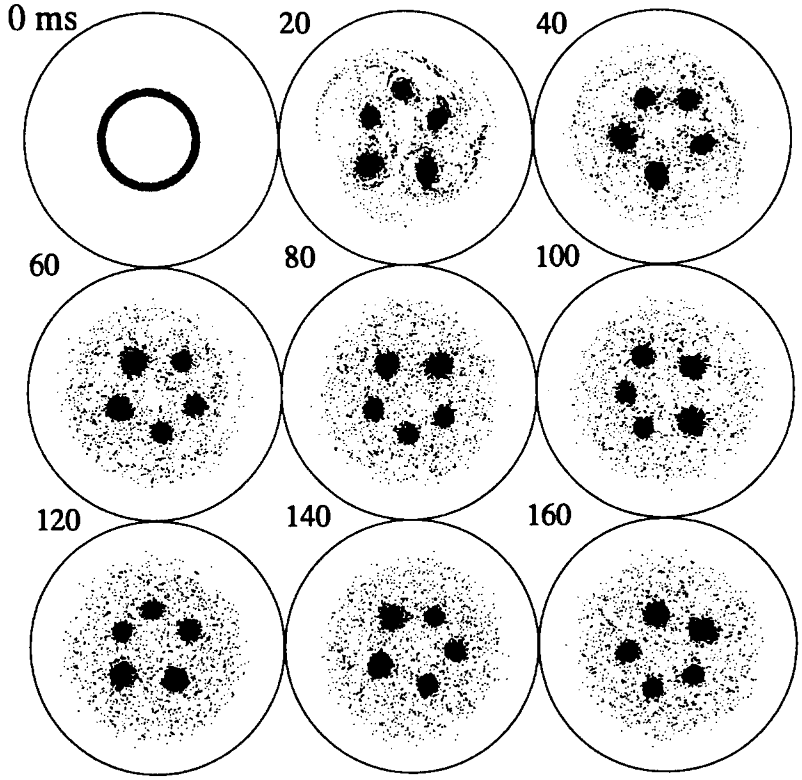

Fig. 13. Long time-scale dynamics of a hollow beam ion cloud to a vortex crystal state. The outer and inner radii of the initial charge distribution are 1.0 and 0.85 cm, respectively. All other parameters are the same as given in Fig. 11.

demonstrate a simple application of measuring the difference in induced charge between two opposing detection electrodes using Eq. (8). In the PIC simulation a relatively large ion cloud (0.5 cm radius) initially located at the trap center (5 cm square cross-section) is first thermalized to 300 K by ion-neutral collisions with 1.5 mtorr He applied for 2 ms. Subsequently, the collision gas is removed with the ion cloud remaining in a 300-K thermal equilibrium state. The ion cloud consists of 2×10^4 simulation particles (m/z 100), each with 150 e charge for a total charge of 3×10^6 e in the ion cloud. This ion cloud, therefore, models 3×10^6 singly charged m/z 100 ions. The ion cloud is excited to a coherent cyclotron radius by applying a linear dipolar chirp electric field which is swept from m/z 300 to m/z 50 in 150 μs. The post-excitation signal, calculated using Eq. (8), is followed for 9 ms. The time step used in the simulations is 0.16 μs. Approximately 61×10^3 time steps are used in each simulation requiring about 7 h of CPU time on a RISC 6000 workstation.

The Fourier transform magnitude spectra of the detected signals are plotted in Fig. 14 for two different simulation runs corresponding to different coherent cyclotron radii. In Fig. 14a and b, the coherent cyclotron radii are 0.375 cm and 1.5 cm, respectively. Negligible damping of the transient and coherent cyclotron motion were observed in the simulations. The large cloud radius was chosen to demonstrate that coherent cyclotron motion is stable for a single m/z even when the coherent cyclotron radius is smaller than the ion cloud radius. While a large radius ion cloud is used in these simulations, this is not a requirement of the PIC method. Additional simulation runs using ion clouds with radii as small as 0.1 cm have been carried out, showing similar results. In particular, the PIC simulation method can be reliably used for any size ion cloud which is greater than one computational mesh cell width (~0.04 cm for the parameters used here, i.e. 128×128 grid and 5 cm trap width), corresponding to the spatial resolution limit owing to a simulation particle's finite size.

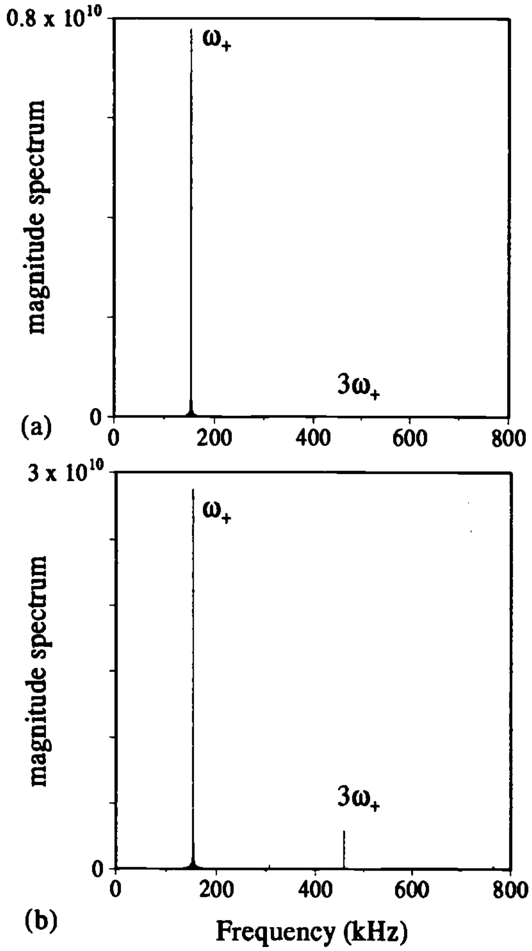

Fig. 14. Fourier transform magnitude spectra of the differential charge induced on opposing detection plates for an m/z 100 ion cloud whose coherent cyclotron radius is (a) 0.375 cm and (b) 1.5 cm. An initially cold ion cloud consisting of 3×10^6 e total charge and radius 0.5 cm is initially placed at the center of a square boundary trap whose edge length is 5 cm. The cloud is thermalized to 300 K by collisions with a 1.5 mtorr He bath gas for 2 ms. Subsequently, the cyclotron motion is coherently excited by a linear dipolar frequency sweep excitation, then detected for 9 ms. Other parameters include $B = 1$ T, 20×10^3 simulation particles each carrying 150 e charge and m/z 100, a 128×128 xy computational mesh, and a 0.16-μs time step.

Fig. 14a represents an ion cloud whose cyclotron radius (0.375 cm) is less than the radius of the ion cloud (0.5 cm). A movie of the particle positions and the detected signal indicated negligible damping or loss of coherence for this ion cloud over the 9 ms transient. The magnitude spectrum shows the effective cyclotron frequency

ω_+ (very close to qB/m since there is no applied trap potential). There is very little third harmonic for such a small cyclotron radius/trap width ratio. Fig. 14b is the magnitude spectrum for a simulation run where the coherent cyclotron radius is 1.5 cm, which corresponds to 60% of the maximum allowed radius. The third harmonic $3\omega_+$ is much larger for this case owing to the non-linearity of the detection circuit which is greater at larger cyclotron radii relative to the trap width ratios [28]. The ratio of third harmonic to first harmonic amplitudes in Fig. 14b is approximately 0.1. In comparing the relative frequency of the fundamental between Fig. 14a and b, we find that ω_+ is down-shifted at higher cyclotron radii due to the image charge interaction in a magnitude which is consistent with simple line charge models for the image charge. Transients considerably longer than 9 ms, corresponding to about 1400 cyclotron periods, are required in order to make detailed comparisons with theoretical models, owing to the small magnitude of the frequency shift (~ 50 Hz) compared to the spectral peak width (~ 110 Hz).

Two important quantities in our simulations are the total energy and angular momentum about the magnetic field. These quantities provide benchmarks with which to test the reliability of the simulation. Fig. 15 plots the post-excitation histories of various quantities extracted from the simulation described in Fig. 14b for the 20000 particle ion cloud whose coherent cyclotron radius is ~ 1.5 cm and number density is 7.6×10^5 cm^{-3}. Of particular interest are the total energy E_{tot} and the total canonical angular momentum about the magnetic field L_z. Both E_{tot} and L_z are expected to be nearly conserved (during the time intervals where ion-neutral collisions are absent) and provide a test to the accuracy of physical predictions made by our particle simulators. The total energy is the sum of the total kinetic and the total electrostatic energies,

$$E_{\mathrm{tot}} = \sum_k \frac{1}{2} M_k v_k^2 + \int \frac{1}{2} \rho \Phi d\tau \qquad (9)$$

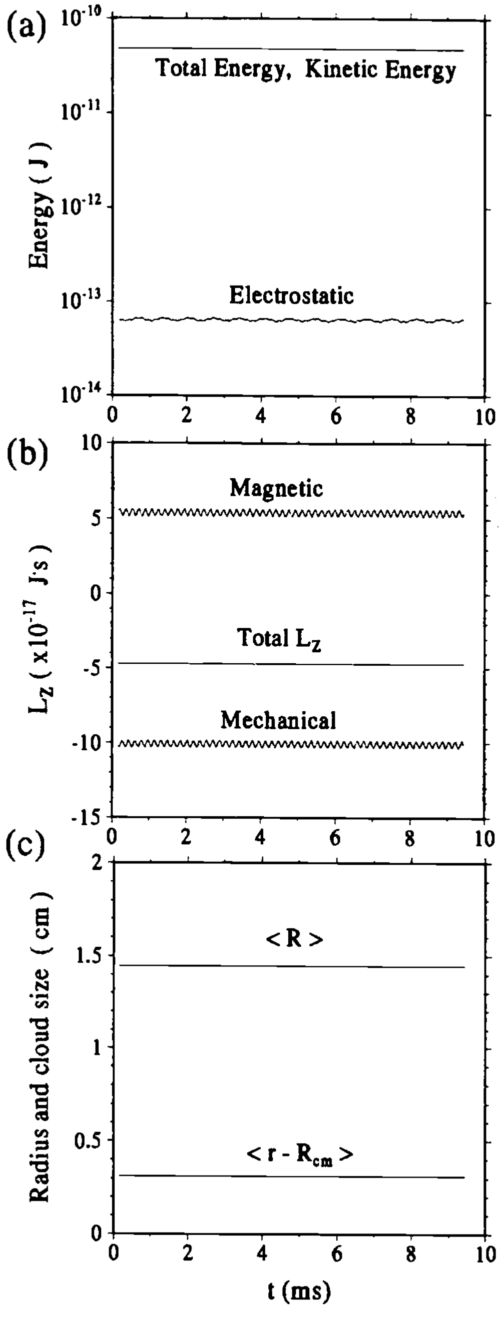

Fig. 15. Time dependence of various quantities for the post-excitation simulation run described in Fig. 14b. (a) Kinetic, electrostatic and total energies; (b) mechanical, magnetic and total angular momenta about the z-axis; and (c) ensemble-averaged coherent cyclotron radius $\langle R \rangle$ and mean particle-center of mass separation $\langle r - R_{\mathrm{cm}} \rangle$.

The kinetic energy s
where v_k and M_k
the kth simulation
simulation conditio
$M_k = 15\,000$ u since
resents 150 single io
on the right in Eq.
where ρ, Φ and dτ
trostatic potential,
tively. The electro
evaluated by replac
a summation over g
i and j are grid ind
element dτ by the
Lh^2.

The total, kinetic
plotted in Fig. 15a
ensemble. The kine
the electrostatic e
large cyclotron ra
served to within 0.
strating very good

The second pro
canonical angular
field, called total
two individual con

$$L_z = \sum_k M_k(r_k \times v$$

where the summat
tion particles and
tained in the kth
and second contri
of Eq. (10) are the
angular momenta
are plotted in Fig.
try is cylindrically
conserved quantit
Fig. 14 employed
tion which inval
conservation argu
over an observati
ods the total ang
better than 0.1%,

The coherent
stable for these

The kinetic energy summation is over all particles where v_k and M_k are the velocity and mass of the kth simulation particle, respectively. For the simulation conditions used here (see Fig. 14b), $M_k = 15\,000$ u since each simulation particle represents 150 single ions of mass 100 u. The integral on the right in Eq. (9) is the electrostatic energy, where ρ, Φ and $d\tau$ are the charge density, electrostatic potential, and volume element, respectively. The electrostatic energy is numerically evaluated by replacing the integral in Eq. (9) with a summation over grid variables ρ_{ij} and Φ_{ij}, where i and j are grid indices, and replacing the volume element $d\tau$ by the volume of a computational cell Lh^2.

The total, kinetic and electrostatic energies are plotted in Fig. 15a for the post-excitation particle ensemble. The kinetic energy is much larger than the electrostatic energy owing to the relatively large cyclotron radius. The total energy is conserved to within 0.01% in this simulation demonstrating very good energy conservation.

The second property of interest is the total canonical angular momentum about the magnetic field, called total L_z. The total L_z is the sum of two individual contributions,

$$L_z = \sum_k M_k (r_k \times v_k)_z + \frac{B}{2} \sum_k Q_k r_k^2 \tag{10}$$

where the summations are over all of the simulation particles and Q_k is the total charge contained in the kth simulation particle. The first and second contributions on the right hand side of Eq. (10) are the mechanical and magnetic field angular momenta, respectively. These quantities are plotted in Fig. 15b. If the confinement geometry is cylindrically symmetric, then L_z should be a conserved quantity. However, the simulations in Fig. 14 employed a trap with a square cross-section which invalidates the angular momentum conservation argument. It is very interesting that over an observation time of 1400 cyclotron periods the total angular momentum is conserved to better than 0.1%, even with our use of a box trap.

The coherent cyclotron motion is remarkably stable for these single m/z simulations, an observation which attests to the ability of particle-in-cell simulations to accurately follow the cyclotron dynamics of tens of thousands of particles over very long detection periods. Two quantities which characterize the relative stability of the particle ensemble are the coherent cyclotron radius and the ion cloud size. For an ensemble of N particles with cyclotron frequency ω_c, the coherent cyclotron radius is given by

$$\langle R \rangle = \frac{1}{N\omega_c} \sqrt{\left(\sum_{k=1}^{N} v_{xk} \right)^2 + \left(\sum_{k=1}^{N} v_{yk} \right)^2} \tag{11}$$

where v_x and v_y are the velocity components of the kth particle. A relative measure of an ion cloud's size is given by the mean particle displacement from the cloud's center of mass R_{cm}

$$\langle r - R_{cm} \rangle = \frac{1}{N} \sum_{k=1}^{N} | r_k - R_{cm} | \tag{12}$$

This measure is proportional to and less than the ion cloud radius. If $\langle r - R_{cm} \rangle$ is time invariant, then the ion cloud radius is also constant. On the other hand, if the ion cloud expands during the detection period, then $\langle r - R_{cm} \rangle$ increases with time.

Fig. 15c plots the coherent cyclotron radius $\langle R \rangle$ and the mean particle position-center of mass separation distance $\langle r - R_{cm} \rangle$ during the post-excitation trajectory for the many particle simulation. Both of these quantities remain virtually invariant during the 9 ms detection period, partially demonstrating the reliability of the particle-in-cell method and the leap frog integration scheme to accurately follow the dynamics of realistic numbers of interacting particles which have undergone cyclotron resonance.

4. Concluding remarks

The particle-in-cell method solves the Coulombic many body problem with a computational effort that scales linearly with the number of interacting particles. This method accurately simulates the behavior of space charge in realistic devices since the potential is correct at the device electrodes. Elastic ion-neutral collisions are included by the Monte-Carlo method. It is possible to carry out realistic computer experiments with the PIC simulation method which are complimentary to laboratory experiments since PIC includes the combined effects of externally applied fields, Coulombic interactions between large numbers of interacting particles and image charge effects, with very little approximation.

The two dimensional PIC codes described in this work, *rz*PIC and *xy*PIC, have been applied to a number of examples of relevance especially to ICR, including the maximum number of ions which can be confined in a cylindrical trap, collisional cooling in a combined trap, image charge and internal ion cloud induced $E \times B$ drifts in an off-axis ion cloud, vortex merger, Kelvin-Helmholtz instability, and cyclotron resonance.

Space charge sets limits to the maximum number density and maximum total charge which can be confined in an ICR trap. The maximum number density which can be achieved in FT-ICR is the Brillouin limit which is proportional to B^2/m [34,42]. The maximum total charge which can be confined in an ICR trap is determined by the condition that the space charge potential cannot exceed the depth of the confinement potential. Particle simulations demonstrate good agreement with this simple model. In particular, the maximum total charge which can be confined in a cylindrical trap (trap symmetry axis coincides with the cylindrical charge distribution symmetry axis) is directly proportional to the trapping well depth and is independent of the magnetic field under most typical conditions. These typical ICR conditions are that the magnetic field and trapping well depth are sufficiently high and shallow, respectively, that the ion cloud reaches the trap electrodes before the ring electrode if ions are continually introduced into the trap.

Simulations demonstrate that as the trap fills to capacity with ions, the space charge potential cancels the trap potential. This process is shown in Fig. 4. At high space charge conditions the approximately quadrupolar potential for a cylindrical ICR trap is modified by the space charge potential to a particle-in-a-box potential along the *z*-axis. At the *z*-confinement limit, the trapping well potential is exactly cancelled by the space charge potential along the *z*-axis. Since the cylindrical (*rz*) particle-in-cell simulation code was applied to cylindrically symmetric systems, the two-dimensional results are identical to three-dimensional, by symmetry.

The Cartesian (*xy*) particle-in-cell simulator was applied to the dynamics of extended charge columns confined by a long grounded confinement geometry aligned parallel to an applied magnetic field. A single off-axis charge column revolves around the trap symmetry axis and its own symmetry axis owing to image charge and internal Coulomb $E \times B$ drift, respectively. The measured drift frequencies from the simulations are in quantitative agreement with analytical models.

The exact isomorphism between two dimensional $E \times B$ dynamics and the Euler equations describing an incompressible inviscid two dimensional fluid have recently been exploited in non-neutral plasma experiments [24–27]. We have carried out numerical simulations on two off-axis charge columns demonstrating vortex merger for sufficiently close separation distances. The critical separation distance for vortex merger to occur is found to be in quantitative agreement with experiment. In addition, we have carried out a series of simulations on hollow beam initial charge distributions. Hollow distributions break apart into a number of vortices owing to Kelvin-Helmholtz instability. The number of vortices created at the initial onset of instability, is found in the simulations to increase approximately linearly with the ratio of the distribution radius divided by the distribution thickness, in reasonable agreement with experiment [26]. An unexpected result of our simulations on hollow beam distributions is that the long time scale dynamics of a sufficiently thin ring ion cloud may evolve to a vortex crystal state, characterized by a relatively small number of high density vortices geometrically arranged on a near uniform low density background vorticity. Experiments have recently observed vortex crystals, which may represent a new metastable near inviscid fluid equilibrium [27].

Acknowledgemen

We thank Drs.
wood for discussi
This research w
west National L
Associated West
lowship. This w
Department of
nal Laboratory i
Institute throug
1830.

References

[1] F.A. Londry, R
Spectrom. 4 (1
[2] R.K. Julian, M.
Mass Spectrom
[3] R.K. Julian, H
Spectrom. Ion
[4] Y. Wang, J. Fr
trom. Ion Proc
[5] B.A. Hearn, C.
Mass Spectrom
[6] G.T. Uechi, R.
(1992) 734.
[7] N.V. Miluchihi
Mass Spectrom
[8] E.N. Nikolaev,
Spectrom. Ion
[9] X. Xiang, S. C
Spectrom. 5 (1
[10] A.J. Peurrung,
Processes 145 (
[11] D.W. Mitchell,
771.
[12] D.H.E. Dubin,
511.
[13] J. Barnes, P. H
[14] F.H. Harlow. M
[15] C.K. Birdsall,
puter Simulatio

Acknowledgements

We thank Drs. Harold Udseth and Alan Rockwood for discussions on the subject of this paper. This research was carried out at Pacific Northwest National Laboratory and supported by an Associated Western Universities postdoctoral fellowship. This work was supported through the Department of Energy. Pacific Northwest National Laboratory is operated by Battelle Memorial Institute through contract DE-AC 0676RLO-1830.

References

[1] F.A. Londry, R.L. Alfred, R.E. March. J. Am. Soc. Mass Spectrom. 4 (1993) 687.
[2] R.K. Julian, M. Nappi, C. Weil, R.G. Cooks. J. Am. Soc. Mass Spectrom. 6 (1995) 57.
[3] R.K. Julian, H.-P. Reiser, R.G. Cooks. Int. J. Mass Spectrom. Ion Processes 110 (1991) 159.
[4] Y. Wang, J. Franzen, K.-P. Wanczek. Int. J. Mass Spectrom. Ion Processes 124 (1993) 125.
[5] B.A. Hearn, C.H. Watson, G. Baykut, J.R. Eyler. Int. J. Mass Spectrom. Ion Processes 95 (1990) 299.
[6] G.T. Uechi, R.C. Dunbar. J. Am. Soc. Mass Spectrom. 3 (1992) 734.
[7] N.V. Miluchihin, K. Miura, M. Inoue. Rapid Commun. Mass Spectrom. 7 (1993) 966.
[8] E.N. Nikolaev, N.V. Miluchihin, M. Inoue. Int. J. Mass Spectrom. Ion Processes 148 (1995) 145.
[9] X. Xiang, S. Guan, A.G. Marshall. J. Am. Soc. Mass Spectrom. 5 (1994) 238.
[10] A.J. Peurrung, R.T. Kouzes. Int. J. Mass Spectrom. Ion Processes 145 (1995) 139.
[11] D.W. Mitchell, R.D. Smith. J. Mass Spectrom. 31 (1996) 771.
[12] D.H.E. Dubin, T.M. O'Neil. Phys. Rev. Lett. 60 (1988) 511.
[13] J. Barnes, P. Hut. Nature 324 (1986) 446.
[14] F.H. Harlow. Methods Comp. Phys. 3 (1964) 319.
[15] C.K. Birdsall, A.B. Langdon. Plasma Physics via Computer Simulation, McGraw-Hill, New York, 1985.
[16] C.K. Birdsall. IEEE Trans. Plasma Sci. 19 (1991) 65.
[17] J.M. Dawson. Rev. Mod. Phys. 55 (1983) 403.
[18] R.W. Hockney. Methods Comp. Phys. 9 (1970) 135.
[19] R.W. Hockney, J.W. Eastwood. Computer Simulation Using Particles, Adam Hilger, New York, 1988.
[20] A.L. Melott, S.F. Shandarin. Astrophys. J. 410 (1993) 469.
[21] H. Ramachandran, G.J. Morales, V.K. Decyk. Phys. Fluids B 5 (1993) 2733.
[22] G.W. Mason, R.L. Spencer, J.A. Bennett. Phys. Plasmas 3 (1996) 1502.
[23] R.W. Hockney. J. Appl. Phys. 39 (1968) 4166.
[24] C.F. Driscoll, K.S. Fine. Phys. Fluids B 2 (1990) 1359.
[25] K.S. Fine, C.F. Driscoll, J.H. Malmberg, T.B. Mitchell. Phys. Rev. Lett. 67 (1991) 588.
[26] A.J. Peurrung, J. Fajans. Phys. Fluids A 5 (1993) 493.
[27] K.S. Fine, A.C. Cass, W.G. Flynn, C.F. Driscoll. Phys. Rev. Lett. 75 (1995) 3277.
[28] P.B. Grosshans, P.J. Shields, A.G. Marshall. J. Chem. Phys. 94 (1991) 5341.
[29] X. Xiang, P.B. Grosshans, A.G. Marshall. Int. J. Mass Spectrom. Ion Processes 125 (1993) 33.
[30] M.V. Gorshkov, A.G. Marshall, E.N. Nikolaev. J. Am. Soc. Mass Spectrom. 4 (1993) 855.
[31] T.M. O'Neil, R.A. Smith. Phys. Fluids B 4 (1992) 2720.
[32] R.W. Hockney. Phys. Fluids 9 (1966) 1826.
[33] D.W. Mitchell, R.D. Smith. Phys. Rev. E 52 (1995) 4366.
[34] L. Brillouin. Phys. Rev. 67 (1945) 260.
[35] P.N. Swartzrauber. SIAM Rev. 19 (1977) 490.
[36] P.N. Swartzrauber, R. Sweet. 'Efficient FORTRAN Subprograms for the Solution of Elliptic Equations', NCAR TN/IA-109, July 1975, 138 p.
[37] R. Sweet. SIAM J. Num. Anal. 14 (1977) 706.
[38] O. Buneman. J. Comp. Phys. 1 (1967) 517.
[39] C.F. Driscoll. In: D. Cline (Ed.), Low Energy Antimatter, World Scientific, Singapore, 1986, p. 184.
[40] D.L. Rempel, M.L. Gross. J. Am. Soc. Mass Spectrom. 3 (1992) 590.
[41] R.E. March, R.J. Hughes. Quadrupole Mass Spectrometry, John Wiley, New York, 1989.
[42] J.J. Bollinger, D.J. Wineland, D.H.E. Dubin. Phys. Plasmas 1 (1994) 1403.
[43] A.J. Peurrung, R.T. Kouzes. Phys. Rev. E 49 (1994) 4362.
[44] R.C. Dunbar. Int. J. Mass Spectrom. Ion Processes 56 (1984) 1.